Journal of Hydrology 664 (2026) 134379

Contents lists available at ScienceDirect

Journal of Hydrology

journal homepage: www.elsevier.com/locate/jhydrol

Research papers

Water tracer model-assessed contributions of source waters to changing circumpolar Arctic terrestrial evapotranspiration and river discharge

Hotaek Park [a,b,*], Youngwook Kim [c], John Gibson [d], Tetsuya Hiyama [b]

[a] Institute of Arctic Climate and Environmental Research, JAMSTEC, Yokosuka, Japan
[b] Institute for Space–Earth Environmental Research, Nagoya University, Nagoya, Japan
[c] Biology Department, College of Science, United Arab Emirates University, Al Ain, United Arab Emirates
[d] InnoTech Alberta, Victoria, BC, Canada

ARTICLE INFO

This manuscript was handled by Amilcare Porporato, Editor-in-Chief

Keywords:
Source waters
Water tracer model
River discharge
Evapotranspiration
Circumpolar Arctic rivers

ABSTRACT

Climate change has resulted in alteration of snow cover, permafrost degradation, vegetation infilling, and precipitation apportionment across the Arctic terrestrial region, which has in turn affected the balance of hydrological processes including seasonality and interaction of snowmelt, rain, and soil water storage. Effects on Arctic river discharge have been widely observed, although relatively few studies have provided detailed assessments of the underlying causes of change, including adjustments in the timing and relative contributions of source waters (i.e., snowmelt, rainwater, soil water, permafrost thaw) and the effects of altered evapotranspiration regimes. Principal challenges have included limitations in the observational networks, which have often frustrated efforts to reliably model complex changes that are underway. This study explores a tracer-aided ecohydrological model that was used to quantitatively assess source water contributions to evapotranspiration and discharge from the circumpolar Arctic river basin, based on three meteorological forcing datasets from the period of 1979 to 2016. The model, which provides additional constraints on water partitioning using isotopic evidence, revealed that rain and snowmelt water accounted for 67% and 39% of the annual evapotranspiration and discharge averaged over the study period, respectively. Rainwater contributions to annual evapotranspiration and discharge were found to have increasing trends over the study period, whereas snowmelt water showed fairly stable or insignificant negative trends. Rainwater was determined to be a dominant source of evapotranspiration across the growing season, while discharge was sustained by seasonally-varying dominant water sources. Earlier snowmelt events also appear to have increased the proportion of snow and rain in peak discharge, with rainwater sources being linked largely to autumn storage in the previous year. We attribute higher evapotranspiration in summer to reduction in the proportion of rain and snowmelt water in summer discharge, resulting in negative interannual trend. Both soil water and permafrost thaw likely have contributed to increases in cold season discharge, although the proportion accounted for by permafrost thaw sources was mostly low. Our analysis renders a new perspective on underlying changes to source water partitioning, especially enhanced rainwater contributions, as a key driver of seasonal, interannual and regional changes in terrestrial evapotranspiration and discharge across the Arctic region.

1. Introduction

Climate change has resulted in air temperature warming across the terrestrial Arctic region, including longer thawing periods above 0℃ and associated increases in evapotranspiration and runoff (Vihma et al., 2016), higher vegetation productivity (Ren et al., 2024), and increases in the proportion of summer rainfall to annual precipitation (Bintanja and Andry, 2017). Both observations and model experiments have suggested increasing trends in Arctic terrestrial evapotranspiration for the past few decades (Rawlins et al., 2010; Zhang et al., 2010; Kotani et al., 2019; Helbig et al., 2020; Park et al., 2021a; Kim et al., 2023). Increased evapotranspiration has mainly been attributed directly to atmospheric warming, given that evapotranspiration is an energy constrained process in the cold regions (Wang et al., 2022), but indirect controls may also be important including factors governing soil moisture deficit. Higher vegetation productivity under the warming climates has

* Corresponding author at: Institute of Arctic Climate and Environmental Research, JAMSTEC, Yokosuka, Japan.
E-mail address: park@jamstec.go.jp (H. Park).

https://doi.org/10.1016/j.jhydrol.2025.134379
Received 23 June 2025; Received in revised form 3 October 2025; Accepted 4 October 2025
Available online 8 October 2025

been shown to be correlated with greater soil water uptake by plant roots, thereby sustaining higher transpiration rates (Park et al., 2021a). Wetter soils, induced by higher precipitation, have been attributed to enhanced runoff (Wang et al., 2021a; Park et al., 2022, 2024), particularly in autumn (Hiyama et al., 2023), and coincident with waning evapotranspiration (Park et al., 2008). While snowmelt water is often an important soil moisture input in spring and early summer, it can remain an important source of evapotranspiration and runoff throughout the growing season (Park et al., 2021a, 2024). On the other hand, some regions have experienced dried soils under the warming climates, in which larger evapotranspiration has been further enhanced seasonal dryness (Lian et al., 2020).

Warming temperatures in the Arctic have resulted in regionally heterogeneous changes in snow depth and cover (Hessilt et al., 2023) with consistently earlier snowmelt in the spring (Mudryk et al., 2017; Park et al., 2024). Earlier snowmelt, and associated decrease in albedo, has in turn resulted in earlier soil thawing and deepening of active layer thickness (ALT; Park et al., 2013, 2015; Kim et al., 2024), as well as advancement in the spring onset of soil evaporation (Park et al., 2022), accompanied by earlier surface drying and often leading to enhanced terrestrial aridity (Park et al., 2022; Hiyama et al., 2023). Although changes in snowmelt timing have different effects on soil water storage in wet and dry climates, the common outcome is often earlier freshet peaks in snowmelt-dominated river watersheds (Shiklomanov et al., 2007; Tananaev et al., 2016; Suzuki et al., 2020; Park et al., 2024). While warmer winter air temperatures in the Arctic have tended to be associated with reduction in snow water equivalents and earlier peak flows (Pulliainen et al., 2020), they have apparently had little impact on discharge volumes (Shiklomanov et al., 2007). As earlier snowmelt often occurs when soil infiltration capacity is limited, there may be associated increases in direct snowmelt runoff (Park et al., 2015; 2024), although little information is available on partitioning of snowmelt contributions to runoff *versus* soil water storage. Likewise, there have been few studies of the specific water sources utilized for evapotranspiration or contributing to discharge during the growing season.

Both observations and model simulations have addressed the trend of deepening ALT over the past several decades (Kim et al., 2012; Park et al., 2013, 2015, 2016a). Increases in ALT augment soil water storage capacity (White et al., 2007; Walvoord and Kurylyk, 2016), also exerting influence on moisture availability, evapotranspiration and discharge (Evans et al., 2020; Wang et al., 2021b), which is a pronounced linkage in wetter climates (Rawlins et al., 2010). Under drier conditions, ALT requires more water to attain saturation, which can diminish the linkage of soil water to runoff. Observations of Arctic river discharge have shown increases in low flow during the cold season, revealing significant correlations with deepening ALT (Smith et al., 2007; Walvoord and Striegl, 2007; Wang et al., 2021b; Han and Menzel, 2022), and potential influence of increased summer rainfall (Hiyama et al., 2023). Permafrost can also store considerable quantities of excess ice (i.e., ice wedge and Yedoma). As ALT deepens, excess ice also melts, wetting the bottom of the active layer, and often promoting baseflow generation (Walvoord and Kurylyk, 2016). Melting of excess ice also leads to the expansion of thermokarst lakes and wetlands. Water balance studies of thermokarst lakes in Central Yakutia, Russia reported that excess ice degradation produced 24–33 % of the total water input to typical growing lakes (Fedorov et al., 2014). The formation of thermokarst lakes may introduce natural sinks that temporarily divert runoff from reaching basin outlets, especially during filling stages. Recent work by Liljedahl et al. (2016) has shown that ice wedge melting leads to overall landscape drying. Quantifying and predicting the effect of permafrost degradation on the Arctic river discharge, which has been shown to produce a cyclic dynamic of water inputs during thaw (Wan et al. 2019a,b, 2020; Gibson et al. 2019, 2025), remains a major challenge for hydrological systems in high-latitude and high-altitude regions.

Overall, previous studies have provided a general perspective on the role of climate warming on spring snowmelt timing, summer rainfall regime, and permafrost-thaw source potential. However, dynamics of individual source waters has not been quantified in detail and is therefore less understood. Enhanced hydrological dynamics during the summer period, as forced by hydro-climatological events, has been observed. However, subtle changes in water budgets are likely masked by complex interactions between individual source waters in the eco-hydrological system. Despite the difficulty, various methodologies have been developed and applied to assess the source water contributions to the hydrological processes. Environmental isotope tracers (i.e., oxygen-18, δ^{18}O; deuterium, δ^{2}H; and tritium, ^{3}H) have been widely applied in process studies to quantify representative source water contributions to streamflow (Amour et al., 2005; Welp et al., 2005; Soulsby et al., 2015; Jasechko et al., 2016; Ala-aho et al., 2018; Allen et al., 2019; Hathaway et al., 2022; Kershaw et al., 2022), and sometimes in combination with hydrochemical tracers (Hoeg et al., 2000; Zhang et al., 2018), to examine origin and residence time of groundwater (Sprenger and Allen, 2020). Stable isotopes have also been applied to estimate the partitioning of *ET* to evaporation and transpiration (Gibson and Edwards, 2002; Jasechko et al., 2013; Aron et al., 2020; Gibson et al., 2020, 2021a; Sprenger et al., 2022). In addition, isotopic analysis of plant water has provided important insight into seasonal or permafrost-derived soil–water sources (Allen et al., 2019; Knighton et al., 2019; Kirchner and Allen, 2020; Tetzlaff et al., 2020; Miguez-Macho and Fan, 2021; Goldsmith et al., 2022; Nehemy et al., 2022).

While tracer measurements have contributed to improved understanding of water source labelling and partitioning in Arctic systems, particularly at the local or subregional scales, and have proven to be informative indicators for quantifying change, use of the method is limited in many cases by data availability and predictive capacity. Capacity of this approach has been extended to some degree through incorporation of isotopic tracer modules within land surface models (Aleinov and Schmidt, 2006; Fischer, 2006; Yoshimura et al., 2006; Sturm et al., 2010; Risi et al., 2016; Hu et al., 2018; Kuppel et al., 2018; Park et al., 2021a). These tracer-aided numerical models have allowed for wider application at scales appropriate for assessing trends across the Arctic region (Birkel and Soulsby, 2015; Ala-aho et al., 2017; Kuppel et al., 2018). As well, event-based tracer model simulations focusing on the catchment scale have offered good examples of their potential value in cold-regions environments when isotopic and hydrologic observations are available (Stadnyk and Holmes, 2023). However, wider observational assessments across the Arctic region have been limited by sparse network coverage.

This study is one of the first to apply a tracer-aided model to the entire Arctic basin, as compared to previous studies carried out at watershed scales (Boucher and Carey, 2010; Ala-aho et al., 2017; Kuppel et al., 2018; Gibson et al., 2021b). The main objective of this study was to quantify the contribution rates of source waters (i.e., snowmelt, rain, permafrost, and soil, Fig. 1) to discharge and evapotranspiration for the circumpolar Arctic river basin system during 1979 to 2016, which builds upon previous tracer-aided model simulations (Park et al., 2021a). Specifically, this study set out to examine the seasonal, interannual, and regional variability of source waters in evapotranspiration and discharge and their responses to changing hydrometeorological conditions. Our hypothesis at the outset was that tracking of the dynamics and interaction of individual water components under changing climate may lead to better understanding of their individual roles in modifying evapotranspiration, discharge and resulting hydrological regimes across the Arctic basin.

2. Methods

2.1. General model description

The CHANGE model (Park et al., 2011, 2018, 2021a), coupled in this study with a water tracer scheme, is a process-based land surface model (LSM) which incorporates a vegetation dynamics model and a

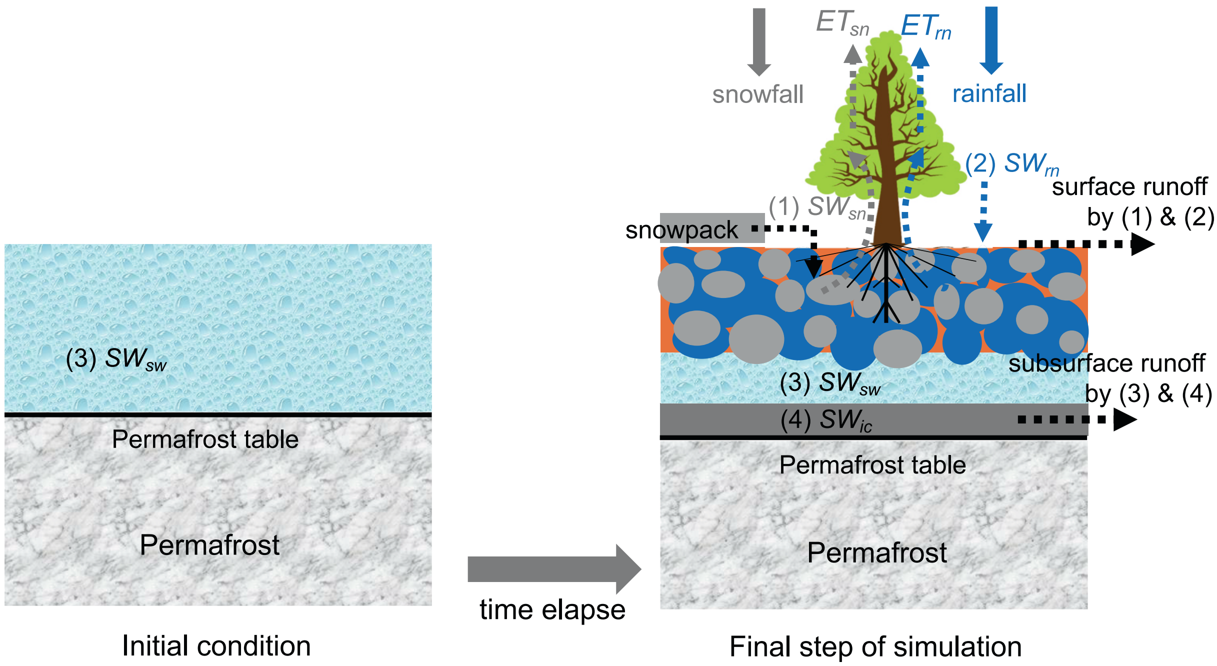

Fig. 1. Schematic illustrating model partitioning of four source waters contributing to *ET* and *Q*. The model was initialized with uniform soil water (left), which was allowed over time to acquire a signature determined by addition of snowmelt and rainfall and losses to *ET* and runoff. Simulated thawing of the active layer drives permafrost-origin water (SW_{ic}) production.

distributed river discharge model, that together simulate water, heat, and carbon fluxes, and plant phenology/physiology in the terrestrial ecohydrological system. The integrated tracer module was previously demonstrated for quantifying contributions of source waters to evapotranspiration in a boreal larch forest, and validated against observational data (Park et al., 2021a). The model simulations provide insight into the responses of the ecosystem processes to atmospheric forcings, as well as interaction and feedback between the terrestrial surface system and atmosphere. Snow is an important variable in the Arctic and subarctic regions. CHANGE simulates the accumulation of snowpack on the land surface during the cold season and the melting and partitioning into surface runoff and soil infiltration in the spring season. The infiltrated snow and rain waters flow up and/or down along water pressure gradients between soil layers, represented by Darcy's law, in which transpiration and drainage are soil–water flux-associated processes. Water fluxes transferred either to the permafrost table or to the bottom soil boundary are defined to be drainage, which is then added to the subsurface runoff. Seasonal freezing and thawing of soils are simulated to capture typical features of soil properties in Arctic and subarctic regions. CHANGE explicitly resolves permafrost dynamics based on hydraulic and thermal principles, considering the soil freezing/thawing phase changes in a soil column of a 50.5-m depth. The CHANGE model also parameterizes permafrost blocking effect on water flow and the effect of soil organic carbon on the soil hydraulic and thermal dynamics, having a profile of vertically distributed carbon content (Park et al., 2015).

In permafrost regions, the soil hydrothermal states affect photosynthesis, stomatal conductance, and plant growth. The fractional increase of ice content in frozen soil layers decreases soil water availability by plant roots, consequently increasing the probability of soil water stress. CHANGE includes a water stress parameter encountered by plants for drying and/or freezing conditions, which is coupled to the maximum rate of carboxylation in leaf photosynthesis and stomatal conductance. CHANGE prognostically treats the carbon and nitrogen cycles in vegetation, crops, and soil biogeochemical processes. These prognostic treatments are consistently utilized to govern carbon and nitrogen state variables in the vegetation, litter, and soil organic matter. The carbon and nitrogen state variables are tracked for leaf, live stem, dead stem, live and dead coarse root, fine root, and grain pools. The seasonal timing of new vegetation growth, including initiation of leaf onset, and litterfall is also prognostic, responding to air and soil temperature, soil water availability, and daylength. The model-estimated leaf area index, stem area index, root amount, and plant heights are utilized by the biophysical module that simulates water, energy, and carbon fluxes. The vegetation dynamics model in CHANGE facilitates the exploration of the bidirectional interactions and feedback between ecosystem and climate.

2.2. Coupling of water tracer scheme to distributed river discharge model

The CHANGE model adopted an upstream isotopic scheme (Aleinov and Schmidt, 2006) to simulate the tracers of the four specified source waters for the components of the water budget in the circumpolar Arctic river basin system. The water budget involving the source waters is expressed as,

$$SW_j = ET_j + Q_j \pm \Delta S_j \tag{1}$$

where *SW* is source water including precipitation, *ET* is evapotranspiration that is consisted of transpiration (E^t), canopy interception (E^i), and soil evaporation (E^s) including snow sublimation (E^{sb}), *Q* is discharge, and *S* is storage. The subscript *j* refers to the respective source waters, i.e., snowmelt, *sn*; rain, *rn*; permafrost-origin *ic*,; and, soil water, *sw*. The tracer scheme utilizes both the water budget of individual elements (i.e., canopy, snow, and soil) and the water fluxes, calculated by LSM scheme (Park et al., 2021a). As such, the simulation permits tracking of tracer masses along the direction of water flow from canopy to snow and then to soil (Fig. 1). The tracer quantity in each water element is updated over time accounting for LSM-calculated water fluxes and the concentration rates of tracer to total water amount. Finally, CHANGE calculates the tracer volumes of the four source waters outputted as *ET* and surface and subsurface runoffs for each time step.

The CHANGE model couples with the storage-based, distributed river routing "total runoff integrating pathways version 2" (TRIP2) model that is based on spatially effective subgrid river flow velocity that acts to represent a realistic travel time (Ngo-Duc et al. 2007). CHANGE-simulated surface and subsurface runoffs are set as inflows to individual storage reservoirs of TRIP2 (Park et al. 2024). The inflow–outflow balance in individual grid cells prognostically dictates water storage within each grid, and the water storage is used to diagnose other variables. The TRIP2 model also includes a river-ice algorithm that simulates seasonal ice formation, growth, and melt, depending on the variability of the river water temperature that is calculated with a one-dimensional advection–diffusion equation, considering heat and water inflows and heat exchange at the air–water interface (Park et al., 2016b, 2017, 2020). One acknowledged shortcoming of the simulations is that regulation by man-made dams affecting downstream discharge is not considered, which leads to considerable overestimations for the spring peak discharge period in the Ob and Yenisey Rivers (Park et al., 2016b).

This study has led to improvement in the CHANGE model, coupling it with the water tracer module to delineate and capture the movement and interactions of the four source waters and their transformation into river discharge. As runoff from the soil system occurs, the tracer scheme in CHANGE calculates the amounts of the four source waters in the runoff based on distributed output from TRIP2 and computes individual tracer content as well as amalgamated tracer content and total discharge for each time step. The water balance of individual source water storages (S_i) in a grid cell of TRIP2 is calculated considering a river ice effect,

$$\frac{dS_i}{dt} = Q_{I,i} + Q_{O,i} + Q_i - \left(\frac{v}{l \times p} \times S_i\right) + \left(\frac{dI_h}{dt} \times l \times w\right) \tag{2}$$

where t is time step, i is index of the specified four source waters, $Q_{I,i}$ is inflows of source waters from the upstream grid boxes, $Q_{O,i}$ is outflow from source water reservoirs, Q_i is inflows calculated by the tracer scheme of CHANGE, v is the velocity, l is the river channel length within the grid box calculated geometrically, p is the meandering ratio, which adjusts the river length, I_h is the ice thickness calculated by the river ice model, and w is river width that has a geomorphological relationship with mean annual runoff. The fifth term on the right-hand side of Eq. (2) represents the change of water volume resulting from changes in ice thickness. As changes in ice thickness occur, the changed ice thickness is converted to water volume in proportion to the fraction of individual source water storages to total river storage, which is then adjusted for individual storage reservoirs. The parameters (e.g., v, l, p, and w) that are derived based on the total river discharge condition are consistently used for the calculation of the source waters, because the source waters move together with the discharging water.

2.3. End-member mixing analysis

The end-member mixing analysis (EMMA) is a method to determine the proportion of each end member (i.e., source waters) in stream water from multiple end members and tracers. EMMA assumes that tracers of the stream water can be explained by the conservative mixing of a finite set of end members (Hooper et al., 1990). Therefore, the end members are chosen with the most extreme points (e.g., A, B, C in Fig. 2) of candidate source water in all water samples collected in the stream. EMMA assumes that (1) end-member sources of the mixing model are conservative, (2) stream water consists of an identifiable number of end-member sources, (3) end-member compositions are distinct for at least one tracer, and (4) end-member compositions are spatiotemporally constant (Hooper et al., 1990). The use of EMMA is generally limited by uncertainties introduced by spatial and temporal variability in end-member concentrations (Delsman et al., 2013). Recently, statistical learning methods (such as maximum likelihood estimation, Bayesian inference, and Probabilistic liner models with Markov chain Monte Carlo algorithm) attempted to quantify uncertainties resulting from the use of field-sampled end-members (Carrera et al., 2004; Delsman et al., 2013; Popp et al., 2019; Beria et al., 2020). However, the approaches including EMMA cannot deal with non-conservative mixing (Christophersen and Hooper, 1992). Thus, tracers that are regarded to be approximately conservative should be included in the candidate

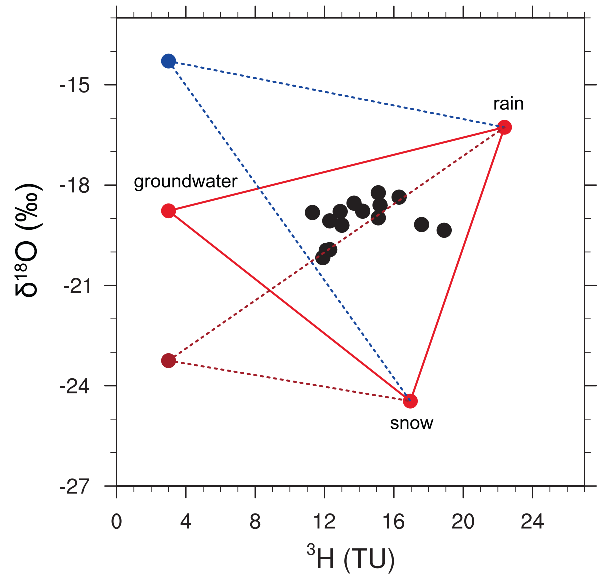

Fig. 2. Tracer ($\delta^{18}O$ and ^3H) concentrations (black dots) observed at Tsiigehthchic station, near the mouth of Mackenzie River, during 2004–2006. End members (red dots, A/B/C) for EMMA analysis were determined based on model results for rain (A) and snow (B) and field data for groundwater (C). Red lines denote mixing between end members. Blue and orange dots denote additional groundwater $\delta^{18}O$ data used to test sensitivity of EMMA model to end member definition. Dotted lines denote mixing between end members.

sources (Delsman et al., 2013). The composition of a source cannot also be identified unless candidate end members are measured. Despite these limitations, EMMA has been widely used for source water separation in many different hydro-climatic and geology settings (Welp et al., 2005; Boucher and Carey, 2010; Blaen et al., 2013; Ala-aho et al., 2018; Allen et al., 2019; Hathaway et al., 2022; Kershaw et al., 2022).

Whitman and Lehmann (2015) introduced a three-source dual-isotope approach that can conclusively partition the river discharge into its three sources. The approach is useful under the conditions that the tracer makeup of river discharge is known, and the three sources have different tracer signatures. The combined pool between the three sources is expressed as,

$$^3H = f_{sn} \cdot {}^3H_{sn} + f_{rn} \cdot {}^3H_{rn} + f_{gw} \cdot {}^3H_{gw} \tag{3}$$

$$\delta^{18}O = f_{sn} \cdot \delta^{18}O_{sn} + f_{rn} \cdot \delta^{18}O_{rn} + f_{gw} \cdot \delta^{18}O_{gw} \tag{4}$$

$$f_{sn} + f_{rn} + f_{gw} = 1 \tag{5}$$

where ^3H and $\delta^{18}O$ are the measured tritium and oxygen-18 isotopic concentrations in river discharge, f is fraction of each source water, the subscript sn, rn, and gw is snow, rain, and groundwater, respectively, and the three tracers of ^3H and δ^{18}O in the right-hand side of Eqs. (3) and (4) are end members of individual source tracers, corresponding to A, B, and C in Fig. 2, which are derived from measurements, as described in the section 2.5.1 later. In the three Eqs. (3)–(5), the fractions of the three sources (i.e., f_{sn}, f_{rn}, and f_{gw}) are unknown, which are mathematically estimated by Bayesian methods using the measured tracer concentrations and determined end members. The equations include ^3H, because it is useful to examine the origin, age, and pathway of groundwater (Jasechko, 2019). The model allowed conclusive partitioning between four source waters. Meanwhile, the EMMA method, described by Eqs. (3)–(5), estimated the fractions of three sources based on the observed isotopic ratios, which included groundwater component unconsidered by CHANGE. We didn't have observational isotopic data for ground ice melting water. Therefore, EMMA considered the groundwater as a source water in the separation, which was compared with water which integrated soil water and permafrost thaw sources as simulated by CHANGE.

2.4. Meteorological forcing data and simulations

The model simulations used different three grided meteorological forcing data that have a global 0.5° latitude/longitude spatial resolution and daily time step covering the period of 1979–2016 [i.e., The WFDEI methodological forcing data applied to ERA-Interim (WATCH), https://doi.org/10.5065/486 N-8109; CRUNCEP Version 7 – Atmospheric Forcing Data for the Community Land Model (CRUNCEP), https://doi.org/10.5065/PZ8F-F017; and Global Soil Wetness Project Phase 3 Atmospheric Boundary Conditions (GSWP), https://doi.org/10.20783/DIAS.501]. The three datasets include the same meteorological variables (e.g., mean, maximum and minimum temperature, surface pressure, specific humidity, precipitation, windspeed, and downward solar and longwave radiation) for forcing model simulations of the study period. The datasets are constructed by combining of a suite of the global observational datasets of the Climatic Research Unit (CRU) with different baseline reanalysis data (i.e., ERA-Interim for WATCH, NCEP-NCAR for CRUNCEP, and 20CR for GSWP) to reduce biases related to low station density and data gaps. To reduce uncertainties associated with any single model forcing, we used different three gridded climatic datasets as inputs for the CHANGE simulations. This study used the average values of results from the three forcing data in the discussion, and the maximum and minimum values among them were defined to be the uncertainty range caused by the meteorological forcing.

The averaged annual snowfall and rainfall of the three meteorological datasets exhibited completely different spatial distributions in the trends (Fig. 3a, b). Snowfall was largely portioned by negative grids (54 %), and the values were statistically insignificant except only certain areas. Meanwhile, the rainfall displayed positive trends over considerable areas (83 %), where the magnitude of the trend was stronger in Siberia than in North America. The tendency of the trends captured at the spatial distributions was extended to the interannual variability. Rainfall significantly increased at the rate of 0.72 mm yr^{-2} ($p < 0.01$), while snowfall showed insignificant negative trend (−0.10 mm yr^{-2}, $p < 0.21$) over the study period (Fig. 3c). Here, snowfall showed larger variations in the annual values between datasets than rainfall, which may represent differences in parameterization that separates precipitation into snowfall and rainfall. Rainfall, averaged over the circumpolar Arctic domain also significantly increased in all months of the growing season (Fig. 3d). The averaged snowfall represented the significant increase in March, while it showed negative values in the growing season, suggesting the impact of the warming air temperature on precipitation partition. In reference, air temperature averaged over the circumpolar Arctic domain indicated increasing trends in annual and monthly scales, although the data were not shown.

The model simulations configured a static land cover classification defined from a global land cover map (Ramankutty and Foley 1999), while the vegetation phenology and physiology were prognostically estimated based on the simulated carbon and nitrogen amounts and surface heat fluxes. Plant roots that extract soil moisture are a major factor resulting in vertically heterogeneous soil water and tracer

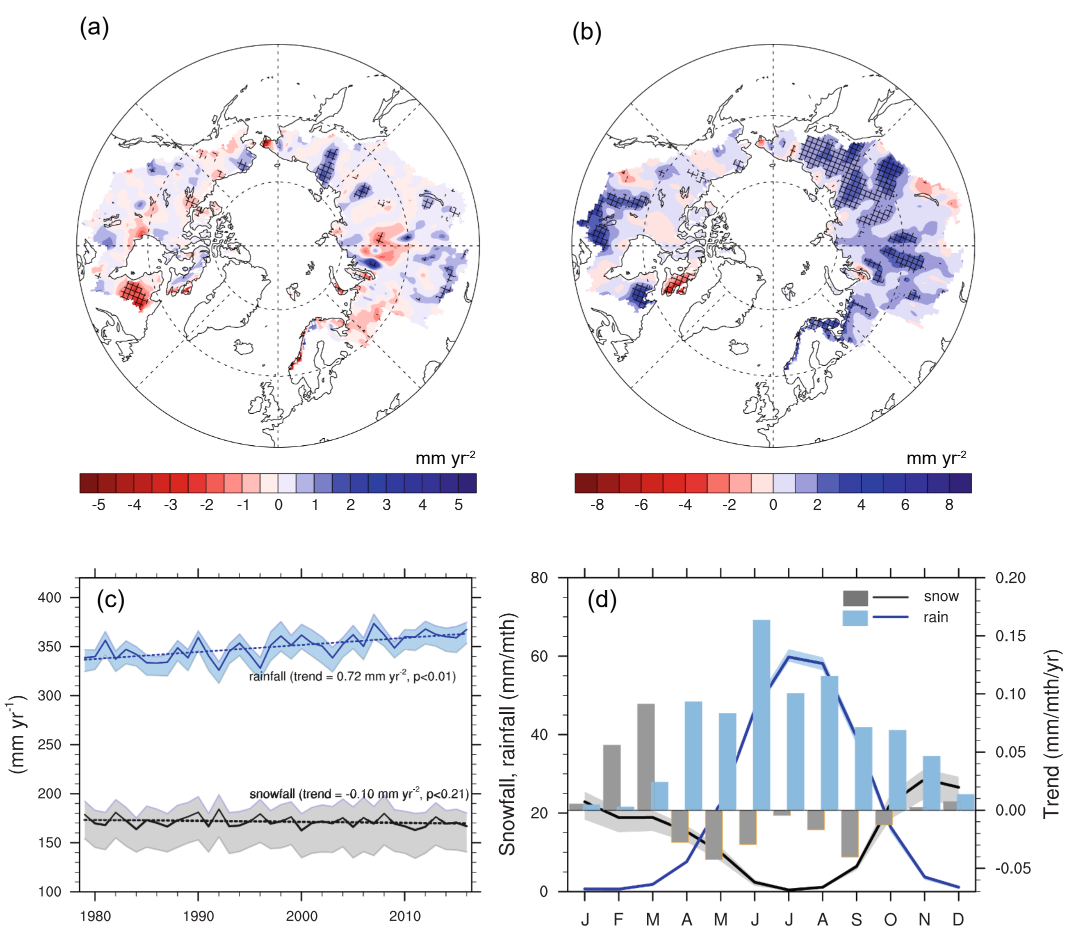

Fig. 3. Spatial distributions and interannual and seasonal variability of snowfall and rainfall. Spatial trend distributions of (a) annual snowfall, and (b) rainfall, from 1979 to 2016, where hatching indicates statistically significant trends at the 90% confidence level. (c) Interannual variability of mean annual rainfall and snowfall, calculated as area-weighted averages by grid cell for the Arctic circumpolar basin. (d) Monthly snowfall and rainfall (lines) and monthly trends during the study period (bars). Shading in panel (c) and (d) illustrates range of maximum and minimum values in individual variables among the three meteorological datasets.

amounts as well as affecting transpiration. CHANGE coupled a dynamic root growth model to estimate changes in vertical root distribution and depth based on the estimated root carbon amount (Arora and Boer, 2003). The dynamic root model can represent sequential responses of roots to changing climatic and hydrothermal conditions and then feedback to other processes (i.e. *ET* and carbon flux). In each grid cell, vertical soil texture fractions for sand, silt, and clay derived from the IGBP SoilData System were used to estimate soil thermal and hydraulic properties.

A spin-up run for 1200 years, repeated with the detrended forcing data of the initial 20 years (Wu et al., 2007) and a CO_2 concentration of 350 ppm, was conducted to determine a dynamic equilibrium of ecosystem carbon and nitrogen states. For the model calculation including spin-up and original runs, it needs the initial values for the four source waters in the soil moisture profile of each grid cell. However, we don't have such dataset covering the pan-Arctic scale. Therefore, volumetric soil water content (0.15 $mm^3\ mm^{-3}$) of each layer set as the initial condition was assumed to SW_{sw}, with the configuration of null values for the remaining source waters. In the case of precipitation events, the precipitation is separated into SW_{rn} and SW_{sn} by the function of air temperature (Park et al., 2024), and they become the inputs of tracer source waters to the LSM elements. Snowmelt and rain waters issued from canopy or snow element were added to SW_{sn} and SW_{rn} in the soil water storages during the spin-up period. The soil water including the source waters was also updated by *ET* and runoff fluxes with snowmelt and rainfall events. The permafrost soil repeats seasonally freezing and thawing, in which the thawing is related to SW_{ic} production. As ALT is larger than the maximum value during the simulation period, including the spin-up run, the water melted from the permafrost soil layer is defined as SW_{ic}. Once the permafrost soil layer thaws, no additional SW_{ic} production does occur from the soil layer. SW_{rn} and SW_{sn} are seasonally freezing and thawing in permafrost soil, especially in the active layers, but the phase changes never affect the change of SW_{ic}. Ultimately, the influence of the initialization of the source waters on the simulation results was minor at least in the active layers (Fig. 1).

2.5. Observational data for model validation

2.5.1. Tracer measurements for determining end members

The Pan-Arctic River Transport of Nutrients, Organic Matter and Suspended Sediments (PARTNERS) project provided seasonal tracer concentration datasets (e.g., $\delta^{18}O$ and ^3H) of discharge measured in the six largest Arctic rivers during 2004–2006 (Yi et al., 2012). We used the measurement of Mackenzie River for validating the model-simulated source waters in discharge. Three source waters (i.e., SW_{sn}, SW_{rn}, and groundwater: SW_{gw}) in river discharge of the Mackenzie River basin were quantitatively separated using the measured discharge tracer data and the EMMA method introduced in the section 2.3. Above all, EMMA needs the tracer end member values of the three source waters (Fig. 2), representing their spatiotemporal variability in the targeted river basin, based on observational data. However, such observational datasets have seldom appeared now, particularly in the isotopic values of groundwater. Thus, the comparison between model simulation and observation was confined to the Mackenzie River possessing the data. We noted model products of regional and global precipitation for $\delta^{18}O$ (Gibson et al., 2020, 2021a,b) and ^3H (Terzer-Wassmuth et al., 2022), respectively, to decide the end members of snowpack and rain waters. The end members of snowpack and rainfall $\delta^{18}O$ were determined by the following steps: precipitation of December–February and June–August was assumed to be snow for snowpack and rain, respectively, and the monthly upstream weighted precipitation $\delta^{18}O$ was averaged to individual seasonal values and then averaged for the observed period. Terzer-Wassmuth et al. (2022) developed a statistical model to simulate globally annual ^3H considering topography and climate. The monthly ^3H data observed at stations in Canada and Alaska since 2000 when the interannual variability of ^3H was not relatively large (Terzer-Wassmuth et al., 2022) were lumped to derive a curve representing the seasonal variation. The seasonal pattern was adjusted to the annual values of all grids in the Mackenzie River basin. ^3H in each grid cell was in turn averaged by the weighting of monthly precipitation to the seasonal total precipitation, and the fraction of each grid area to river basin area was additionally weighted to ^3H and then entirely cumulated. Sublimation from snowpack is a general phenomenon during the winter season, which causes isotopic fractionation resulting in higher snowpack $\delta^{18}O$ value than precipitation. Quantitative information on the fractionation effect at the watershed scale was deficit. Therefore, the fractionation effect was not considered in the determination of the end member. This treatment likely becomes a cause for uncertainties inherent in the EMMA analysis.

We note that observations and model results for global groundwater $\delta^{18}O$ and ^3H are extremely limited compared to precipitation. We gathered published observational data of the groundwater tracers in the Mackenzie River basin (Supplementary Fig. 1), which showed existing data gaps for our study period and larger differences between the limited observational sites (Supplementary Fig. 1). The data deficiencies made it difficult to assign end member signatures *a priori* for the groundwater tracers. Uncertainty was reduced by an assumption; the collected whole tracer data were averaged regardless of the measuring period, which was then substituted into the data deficient study period. In other words, average values were used as end members of $\delta^{18}O$ and ^3H, which is thought to be adequate and representative for periods of a season or longer but may not accurately simulate individual events. The maximum and minimum values of standard deviation from the averaged groundwater $\delta^{18}O$ showed large difference (Supplementary Fig. 1a). As new mixing lines based on the two values were drawn, some observational data in the case of the minimum $\delta^{18}O$ groundwater were situated outside the brown lines (Fig. 2), implying that EMMA likely resulted in abnormal fractions in the separation of source waters for the observations. Additional analyses that the two values set to the end members of groundwater were conducted to assess the sensitivity of EMMA to the end members.

2.5.2. Global ET products

The model-estimated *ET* of this study was compared with five global *ET* datasets to assess the model performance. The global *ET* datasets have different spatial resolutions and data periods. Thus, the assessment between the *ET* products was mainly targeted to the comparison of interannual variability for annual values during the study period, spatially averaged over the circumpolar Arctic river domain. Characteristics of the *ET* products used for the comparison are briefly described below.

- • The Global Land Evaporation Amsterdam Model (GLEAM) uses the Priestley-Tayler equation and the Gash analytical model of vegetation rainfall interception (Miralles et al., 2011). The GLEAM product (v4.2a) provides *ET* and its subcomponents (i.e., soil evaporation, rainfall interception, and transpiration and sublimation) at two spatial–temporal resolutions: 8-day 0.0833° × 0.0833° and daily 0.5° × 0.5° gridded data. The GLEAM *ET* is estimated by the forcing data derived from remote sensing measurements and a synthesis of observation-based precipitation datasets, while considering soil moisture impacts on *ET*.
- • The Global Land Data Assimilation System (GLDAS) provides monthly 0.25° × 0.25° *ET* data, averaging GLDAS-2.1 Noah 3-hourly data simulated by the Noah model 3.3 land information system version 7 (Beaudoing and Rodell, 2016). The forcing data for *ET* estimation include remote sensing-derived *P* and radiation data, and atmospheric analysis model outputs (Jimenez et al., 2011).
- • The Simplified Surface Energy Balance (SSEBop) provides 1-km global *ET* data of three temporal resolutions, including 10-day, monthly, and annual time steps. The SSEBop *ET* data (v61) were estimated by a simplified energy balance approach (Senay et al.,

2013) based on SEBAL (Bastiaanssen et al., 1998) and METRIC (Allen et al., 2007) models, and a thermal index derived from Moderate Resolution Imaging Spectrometer (MODIS) thermal observations.

- • The modified Penman-Monteith (mPM) model produces global daily *ET* estimates at a 9-km resolution, including subcomponents of soil evaporation, canopy interception, and transpiration (Kim et al., 2023). To enhance *ET* estimates, the mPM model incorporates soil moisture constraints on both soil and canopy conductance, using surface and root zone soil moisture data from the National Aeronautics and Space Administration (NASA) Soil Moisture Active Passive (SMAP) mission. The 9-km global daily SMAP mPM ET data records are publicly available for 2016–2021 (https://files.ntsg.umt.edu/data/ET_global_daily_mPM/).
- • The global FLUXCOM-X products are based on observational machine learning model upscaling of *in situ* eddy covariance tower network measurements of surface fluxes (Nelson et al., 2024). The FLUXCOM-X version 4.2a provides *ET* data at two spatial–temporal resolutions: daily at 0.25° × 0.25° and monthly at 0.05° × 0.05°. In this study, annual mean *ET* for the period 2001–2019 was calculated using the monthly 0.05° × 0.05° data to assess inter annual variability.

3. Results

3.1. Evapotranspiration

3.1.1. ET comparison with global ET products

To assess interannual variations, annually averaged total *ET* estimates over the study domain from global data products (SSEBop, GLDAS, GLEAM, and SMAP mPM) were compared against the averaged CHANGE model simulations and aggregated FLUXCOM-X *ET* data. The comparisons showed generally similar interannual *ET* variations in global data products, CHANGE and FLUXCOM-X data, and confirmed significant, positive *ET* trends (0.38–2.36 mm yr^{-2}) (Fig. 4). *ET*s of SSEBop and SMAP mPM showed non-significant decreasing trends in a relatively shorter period of recent years than others including the CHANGE results. The *ET* values of GLEAM, GLDAS, and SSEBop were greater than SMAP mPM, as identified in a previous study (Kim et al., 2023). *ET* values derived from CHANGE were lower than some global products, but relatively close to FLUXCOM-X and SMAP mPM *ET*. Annual mean *ET* estimates derived from three CHANGE model simulations, GLEAM and FLUXCOM-X from 2001 to 2016 show significant positive correspondence across the circumpolar Arctic river basin (r = 0.56 ~ 0.88).

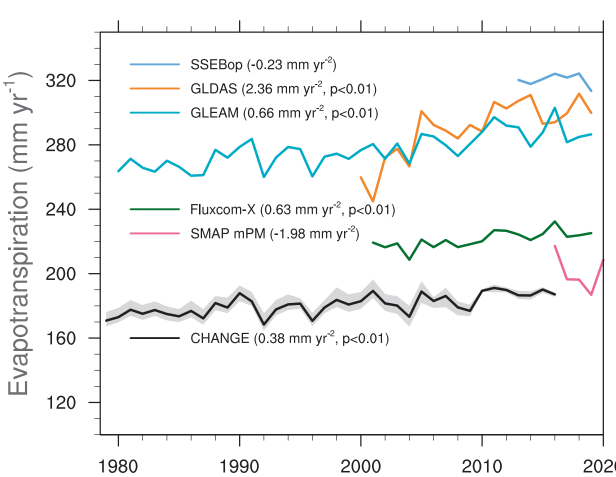

Fig. 4. Interannual variability in mean annual *ET* simulated by CHANGE based on three meteorological datasets (WATCH, CRUNCEP, GSWP) compared to global datasets (SSEBop, GLDAS, GLEAM, Fluxcom-X, SMAP mPM). Trend values and statistics are shown for available time periods. Shading intervals bracketing the CHANGE *ET* trend illustrate maximum and minimum values based on the three meteorological datasets.

3.1.2. Spatiotemporal variability of ET source waters

The CHANGE-simulated annual mean *ET* revealed strong latitudinal gradients, where *ET* values were higher in the southern regions and lower in the north (Fig. 5a), whereas source water contributions to *ET* exhibited regionally different patterns. Relatively higher contribution (i.e., >60 %) of snowmelt water to *ET* (ET_{sn}) was identified for the coldest northern regions of Siberia and Canadian Archipelago, with progressively lower contributions moving toward the southern subarctic regions (Fig. 5b). In contrast, rainwater exhibited higher contributions to *ET* (ET_{rn}) for the southern warm regions and accounted for 50 % or more of *ET* for the entire Arctic basin (excluding the northernmost Siberia and Canadian Archipelago), reaching peak contributions of up to 80 % or more in some southern regions (Fig. 5c). Higher ET_{rn} fractions were closely linked to stronger activity of the *ET* subcomponents during the summer season (Supplementary Fig. 2), characterized by larger rainfall and leaf amounts. Higher rainwater contributions to the *ET* subcomponents (except E^{sb}) were found for subarctic forest-covered regions, accounting for ~ 60 % or more of resulting *ET* (Supplementary Fig. 2). Snowmelt water accounted for the majority of E^{sb} over much of the pan-Arctic regions, with some regional exceptions (Supplementary Fig. 2). The contributions of soil and permafrost-origin waters to *ET* were mostly small and variations were found to be less informative (not shown). The two ground source waters (SW_{sw} and SW_{ic}) generally contributed to soil storage within the lower active layer, below plant rooting depth, as noted in a previous study (Park et al., 2021a). This promoted connectivity of these sources to subsurface runoff rather than to *ET* processes.

3.1.3. Seasonal and interannual variations of ET and source waters

Analysis of seasonal variations in source water contributions to monthly mean *ET* estimated by CHANGE over the circumpolar Arctic domain (Fig. 6) confirmed high contributions of ET_{rn} to the peak summer *ET* (Fig. 6a), with significant increasing trends apparent (0.03 ~ 0.09 mm mth^{-1} yr^{-1}, p < 0.01) during the summer and autumn seasons, among which the largest derived increases appeared for June and then the trend values declined (Fig. 6b). The ET_{sn} trend similarly followed the ET_{rn} seasonal pattern, although the proportion and trend values were found to be considerably muted as compared to ET_{rn}, and negative during July to October. The seasonal trends of *ET* and source waters appear to show notable deviations in August, which appears to reflect moisture limitations at this time of year. Whereas increasing E^i trends were found in August, likely due to greater leaf area, this potentially led to reduction in amount of rainfall reaching soils. The result is expected to be dryer soil conditions, which tend to limit E^t and E^s, although insignificant increases are still found in these fluxes, even in the warming climates (Supplementary Fig. 3b). Evaporation from open water surfaces associated with thermokarst lake and wetland development (Liljedahl et al., 2016; Ulrich et al., 2017) is also an important component of *ET*. However, the CHANGE model did not account for the open water evaporation losses in the simulation, which was likely a cause the underestimation of *ET*.

The circumpolar Arctic annual E^t, assessed by averaging results of the three datasets (Supplementary Table 1), indicated significant increasing trends during the study period (0.39 mm yr^{-2}, p < 0.01), in response to warming air temperature and increasing precipitation (Fig. 3) that induced higher atmospheric evaporative demand and lower soil water stress, respectively. Warming also drives increases in vegetation productivity, and predicts larger leaf areas that contribute to larger E^i (Pan et al., 2020; Yang et al., 2023). Conversely, higher canopy wetting rates by larger interception likely reduces stomatal conductance, which can limit E^t. E^t showed relatively subdued increases (0.09 mm yr^{-2}, p < 0.10) compared to E^i (0.11 mm yr^{-2}, p < 0.01, Fig. 7b), which was likely influenced by significant decreases for southern North America

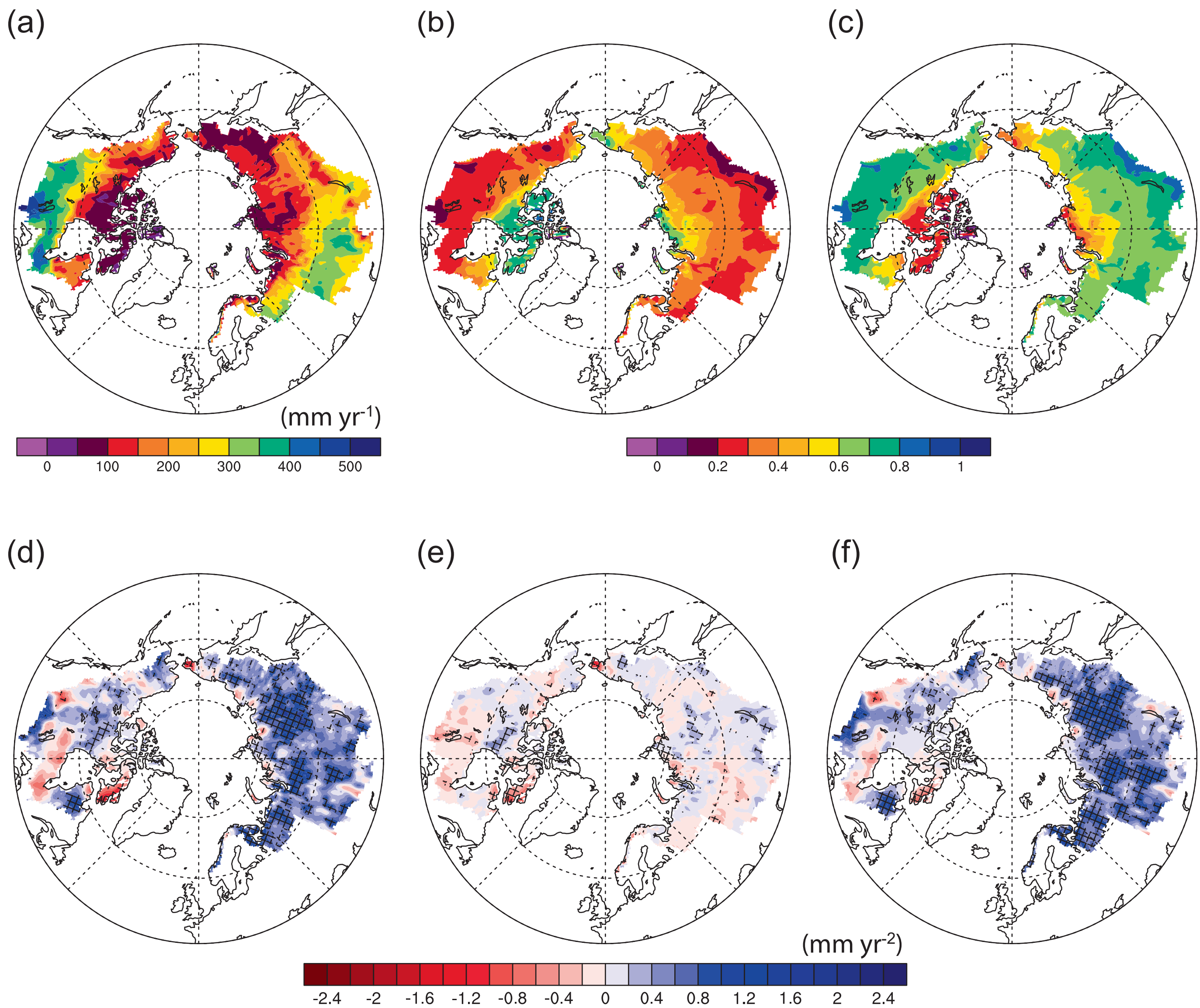

Fig. 5. (Upper panels) Spatial distributions of (a) annual mean *ET*, (b) snowmelt and (c) rainwater contributions to the annual *ET*. (Lower panels) Trends over the study period for (d) annual *ET*, (e) snowmelt water-sourced *ET*, and (f) rainwater-sourced *ET*. Hatching in the trend distributions indicates statistically significant values at the 90% confidence level.

(Supplementary Fig. 2). The increase of E^s was the largest among the *ET* subcomponents (0.20 mm yr^{-2}, $p < 0.01$), which was consistent spatially across the entire circumpolar Arctic domain (Supplementary Fig. 2). Meanwhile, E^{sb}, accounting for 10.0 ~ 11.3 % of *ET* (Supplementary Table 1) showed decreasing trends during the study period (−0.02 mm yr^{-2}, $p < 0.17$), apparently responding to warming winter temperatures. In addition, the winter snow cover period appears to become shortened due to later snow onset in autumn and earlier spring snowmelt (Kim et al., 2017), with reduction in winter snowfall (Fig. 3c), leading to decreases in snowpack water equivalent on the soil surface. These snow conditions likely reduced the quantitative potential for snow sublimation.

The CHANGE-simulated annual mean *ET* also showed a significant increasing trend from 1979 to 2016 (0.38 mm yr^{-2}, $p < 0.01$, Fig. 7a). The increased *ET* was attributable to the impact of ET_{rn} that significantly increased during the study period (0.39 mm yr^{-2}, $p < 0.01$, Fig. 7a) as compared to ET_{sn} that showed little change except perhaps due to minor impact of reduced snowfall (−0.01 mm yr^{-2}, $p < 0.71$; Fig. 7a, 2c). The *ET* subcomponents (e.g., E^t, E^i, and E^s) also showed increasing trends during the study period (Fig. 7b), representing larger use of rainfall during summer season. Rain source water accounted for 70–76 % of the annual E^t, E^i, and E^s (Supplementary Table 1). Soil and permafrost-origin waters in *ET* and the subcomponents accounted for only trace fractions of the total (<1%) with insignificant trends (Supplementary Table 1).

3.1.4. Comparison of ET variables between forcing datasets

The CHANGE-simulated annual *ET* and source waters showed similar interannual variability among the three datasets during the study period (Fig. 7a), with annual mean differences amounting to less than 5 mm (Supplementary Table 1). Similar patterns were also found for *ET* subcomponents (Fig. 7b). The trend values of *ET* and the subcomponents and source waters generally represented similar directions and smaller deviations between the datasets (Supplementary Table 1). Among the three datasets, the CHANGE result forced by GSWP meteorological data recorded the largest trend values in *ET* and other variables among the three datasets, which was most significant for ET_{rn} and subcomponents (Supplementary Table 1). As GSWP incorporates relatively warm summer air temperatures and larger summer rainfall compared to other datasets, this appears to be the consequence.

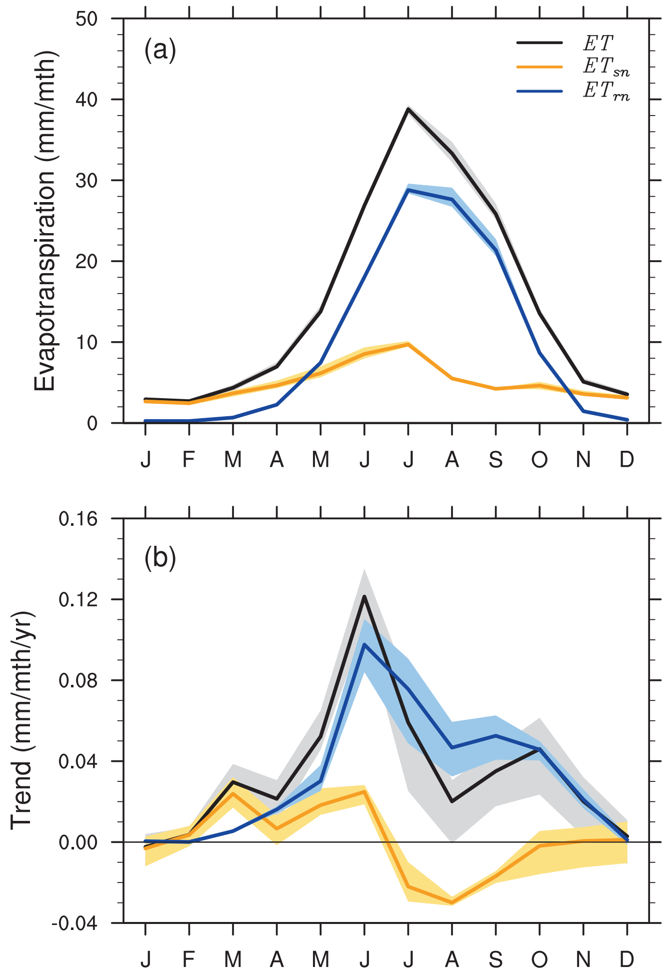

Fig. 6. (a) Seasonal variability of monthly ET and source waters (snowmelt: ET_{sn} and rainwater: ET_{rn}) averaged over the Arctic circumpolar river basin, and (b) trends over the study period. Shading denotes the range of maximum and minimum values produced by the three meteorological datasets.

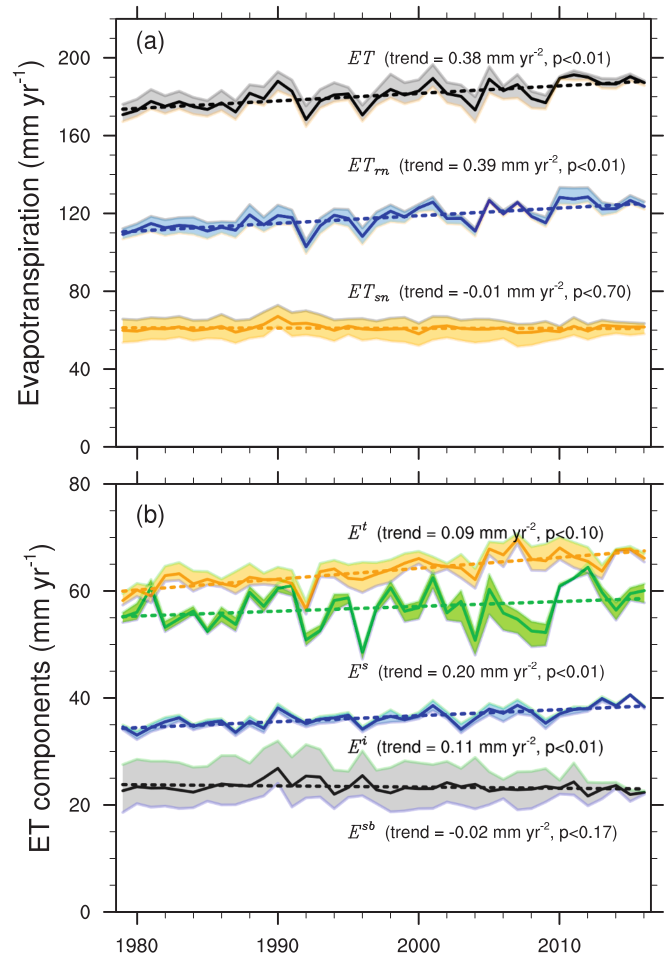

Fig. 7. Interannual variability of (a) annual ET and the source waters (ET_{sn} and ET_{rn}) averaged over the Arctic circumpolar river basin, and (b) ET subcomponents (transpiration: E^t, canopy interception: E^i, soil surface evaporation: E^s, and snow sublimation: E^{sb}). Shading denotes the range of maximum and minimum values produced by the three meteorological datasets.

3.2. River discharge

3.2.1. Comparison of source water discharge against observations

The coupled models, CHANGE and TRIP2, were applied in a previous study to simulate seasonal and interannual discharge from the major Arctic river basins (i.e., Ob, Yenisey, Lena, Kolyma, Yukon, Mackenzie) which found statistically significant agreement between the model and observations (Park et al., 2016b, 2017, 2024; Hiyama et al., 2023). Building upon that work, source water distributions were predicted for discharge, Q, for the Mackenzie River basin and compared with the corresponding variables separated by the EMMA method as well as directly from $\delta^{18}O$ and ^{3}H measurements carried out at the river mouth over three years during summer (Fig. 8). The simulated snowmelt and rainwater-sourced discharges (i.e., Q_{sn} and Q_{rn}) visually showed favorable correspondence with observations, both seasonally and interannually, while agreement for groundwater-sourced discharge (Q_{gw}) was found to be less satisfactory. Seasonal hydrographs for circumpolar Arctic river basins are typically characterized by a pronounced snowmelt-generated peak flow in spring to early summer followed by rapid decline to low flow during late summer to freeze-up. Peak discharge originates nearly exclusively from surface runoff, accounting for 90 % of Q from April to July, while subsurface runoff is found to be the major contributor to Q during late summer and in the cold season (Park et al., 2024). Likewise, our simulations for the Mackenzie River revealed relatively high contributions of Q_{sn} and Q_{rn} to peak Q with snowmelt water being fast linked to spring discharge, but with significant contributions also from Q_{rn} stored from previous years in frozen soils (Fig. 8a, b) which was consistent with expectations and which generally supported the EMMA approach for modelling (see also Hiyama et al., 2023; Park et al., 2024). However, labelling due to evaporative isotopic enrichment inherited from waters residing in surface storage (i.e. wetlands, lakes) is not accounted for in the simulation, which has been shown to be influential for some Arctic rivers including the Mackenzie (Yi et al., 2012, PARTNERS dataset).

In contrast, Q_{gw} showed larger deviations between the observations and model results (Fig. 8c) which indicated that the role of groundwater is underrepresented in the simulations. Note that Q_{gw} is calculated as a mixture of Q_{sw} and Q_{ic} and is intended to represent both supra- and sub-permafrost groundwater (Wang et al., 2024) as well as subsurface flow in non-permafrost regions. Lower than expected variability in the Q_{gw} predictions likely arises from oversimplification of model representation of residence time and mixing of subsurface water sources which control timing of contributions to streamflow, but this can potentially be improved in future through model tuning and customization. We note that the simulated volumetric flux of Q_{gw} appears to vary realistically in terms of relative timing of contributions, which is encouraging.

3.2.2. Spatial variability of discharge source waters

The CHANGE model estimated surface and subsurface runoffs at individual grids and separated source waters in the runoffs, then

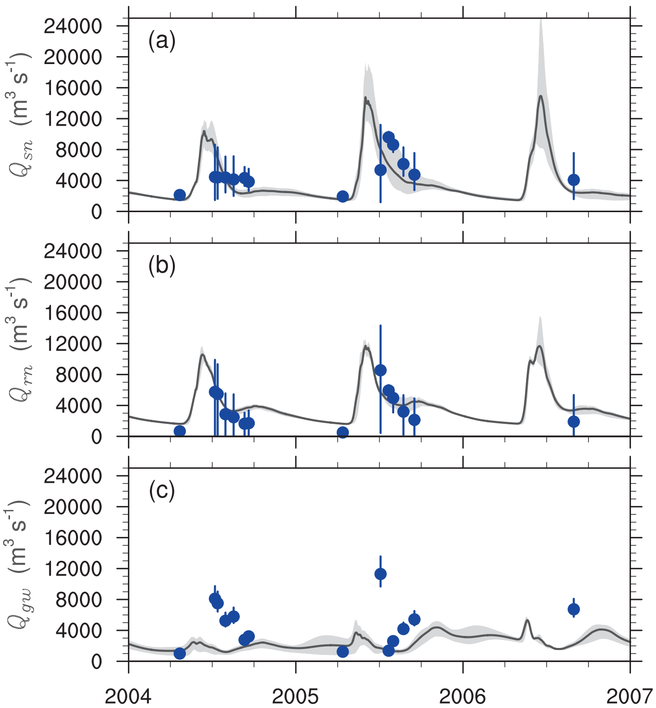

Fig. 8. Comparison of observed (dots) and simulated (lines) source waters in Mackenzie River discharge, including (a) snowmelt, (b) rain, and (c) groundwater. Observed values are based on measured $\delta^{18}O$ and ^{3}H values and inferred separation by EMMA, where vertical lines denote maximum and minimum uncertainty predicted from EMMA sensitivity experiments. Shading denotes the range of maximum and minimum values produced by the three meteorological datasets.

assigned these as inputs to TRIP2 for calculating river discharge along the prescribed river routes. Eq. (2) represents the water assignment from CHANGE to TRIP2 and the water budget in TRIP2. Fig. 9 presents (a) larger spatial variability of the simulated annual mean runoff, (b-e) and fraction of source waters to the annual mean runoff, including (f-j) individual trends during the study period. Higher runoff, recorded annually > 300 mm, was ascertained for northwestern Siberia, east southern Siberia, and northeastern Canada encircling Hudson Bay. The distribution of the separated source waters showed generally higher fractions of snowmelt water in the runoff for large areas of the basin domain, particularly in the northeastern Siberia recording 50 % or more (Fig. 9b). Occurrences of large amounts of rain and snowmelt water-sourced runoff were apparent at the southern boundary of the basin territory (Fig. 9c, d), generally corresponding to discontinuous permafrost or mountainous regions. In comparison, the contribution of permafrost-origin water to runoff was found to be considerably subdued, and generally below 10 % across the entire region where relatively high runoff was identified for the southern discontinuous permafrost regions (Fig. 9e). This is consistent with permafrost thaw being a slow-release process occurring over multiple years.

The annual mean runoff illustrates spatially heterogeneous trend distributions over the domain, but positive values are prevalent (65 %) for larger grids (Fig. 9f). Positive trends tend to be somewhat strengthened for Siberia relative to North America, which may be attributed to rainfall variability (Fig. 3b). Snowmelt and rain waters show generally similar spatial trend patterns, although the trend values are of different magnitudes (Fig. 9g, h), owing to a large portion of the two source waters being active during surface runoff in spring. Soil and permafrost-origin waters also show the similar trend patterns, although their values are different (Fig. 9i, j), as these are tied to fundamental generation of water fluxes unique to conditions of regional soil systems. During a runoff event, both source waters contribute to runoff simultaneously, where the runoff amounts are dependent on respective water storage volumes. This process appears to be consistent for both surface and

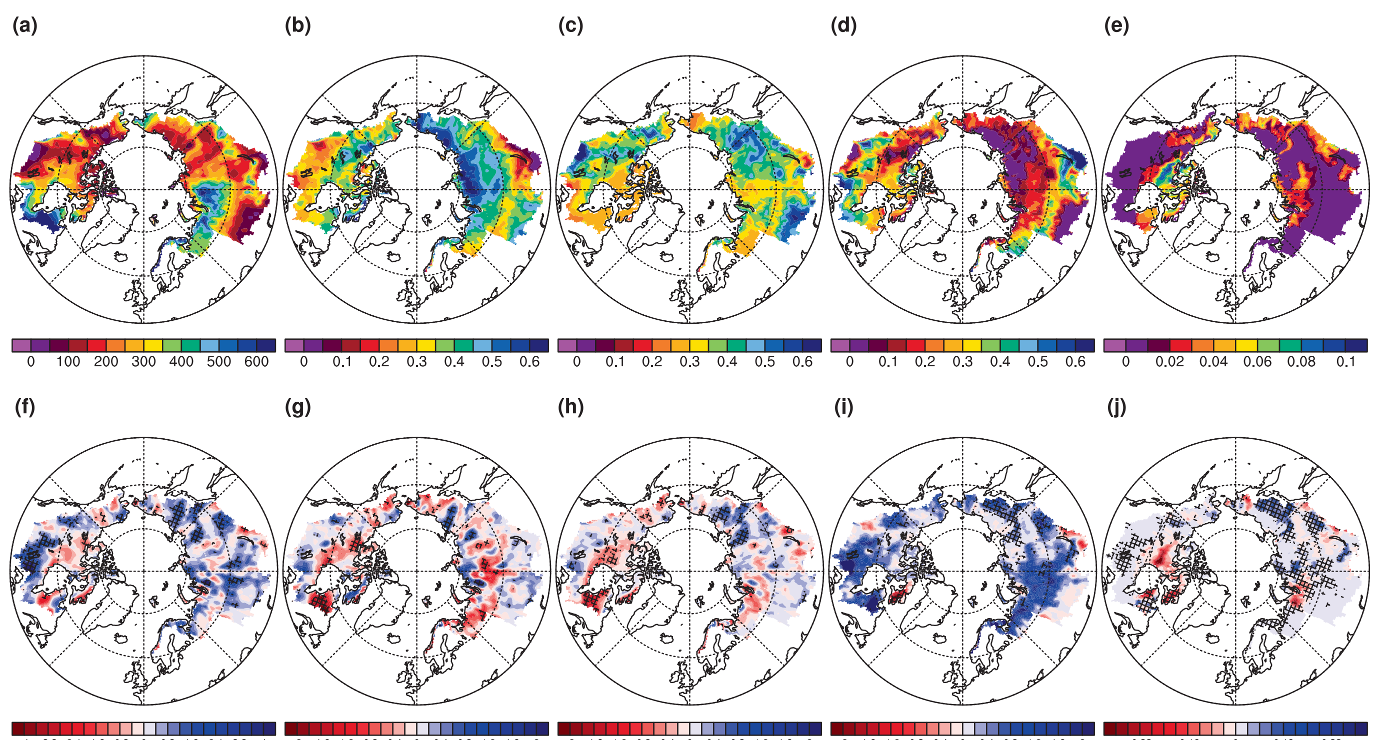

Fig. 9. (Upper panels) Gridded spatial distributions of (a) annual runoff amount (mm yr^{-1}) and annual runoff contributions over the study period derived from (b) snowmelt, (c) rain, (d) soil water, and (e) permafrost thaw sources. (Lower panels) Trends in variables, including (f) annual runoff, and contributions from (g) snowmelt, (h) rain, (i) soil water, and (j) permafrost thaw sources (mm yr^{-2}). Hatching in the trend distributions indicates statistically significant values at the 90% confidence level.

subsurface runoff. Most snowmelt water is directly converted to the spring surface runoff (Park et al., 2024), which serves to limit the mixture of source waters with soil moisture (Park et al., 2021a). As a result, the trend of snowfall is likely influential to the resulting trends in snowmelt water runoff.

3.2.3. Seasonal and interannual variability of discharges

The simulated total discharge from the circumpolar Arctic river basins results in generation of typical seasonal hydrographs, peaking in the spring and early summer and then decreasing (Fig. 10a). Within the seasonal hydrograph, Q_{sn} is found to be a primary contributor to the peak discharge, accounting for 51 % of May–July discharge, during which time Q_{rn} accounted for 39 %. Conversely, in autumn, contributions of Q_{sn} and Q_{rn} to Q were relatively subdued. Instead, Q_{sw}, generated by subsurface runoff, accounted for the majority of autumnal river discharge, even during the freezing season. Although Q_{ic} was quantitatively smallest, its contribution was found to increase slightly during the autumn season when ALT generally reached its maximum. This seasonal pattern suggested that Q_{ic} water was driven along with Q_{sw} by subsurface flow during runoff events, because the waters tended to be distributed within relatively deep soil layers (Park et al., 2021b).

The total Q showed the largest increase of 0.42 km^3 yr^{-1} in early June (Fig. 10b), likely because of earlier snowmelt induced by air temperature warming, as described in previous studies (Suzuki et al., 2020; Hiyama et al., 2023; Park et al., 2024). Abrupt trend reversal in July (-0.37 km^3 yr^{-1}) was likely influenced by the effect of decreased soil moisture due to early onset of snowmelt in addition to enhanced *ET* (Fig. 6b). In general, trends for Q_{sn} and Q_{rn} were consistent with the Q trend, showing similar variations in spring and summer. After August, changes in Q_{sn} and Q_{rn} appear less consequential, although Q_{sw} switches to a weaker increasing phase and appears to maintain positive trends over the cold season, contributing to overall positive Q trends.

Over the course of the study period (1979–2016), the simulated Q from the circumpolar Arctic river basin predicts a significant increasing trend (12.74 km^3 yr^{-2}, $p < 0.01$; Fig. 11), as compared to 11.6 km^3 yr^{-2} observed for circumpolar Arctic rivers Q during a similar period (1984–2018) (Feng et al., 2021). While some difference in magnitude of Q is evident between simulations and observations at the eight major rivers (AMAP, 2025), we note that interannual variability is consistent and well-captured by the simulation ($r = 0.84$, $p < 0.01$), even though the increasing trend (5.95 km^3 yr^{-2}, $p < 0.01$). However, the model exhibits a tendency to overestimate the discharge, likely due to the combined effects of neglecting dam regulation in the discharge calculations and underestimating evaporation from the water surfaces of lakes and wetlands. Q_{sn}, as the dominant contributor to Q (39 %; 4906.0 km^3 yr^{-1}, Supplementary Table 2) showed a negative trend (-0.17 km^3 yr^{-2}, $p > 0.1$), likely due to decreasing snowfall (Fig. 3c). Conversely, Q_{rn}, which accounted for 35 % of the total discharge, show an insignificant increase ($+0.54$ km^3 yr^{-2}, $p > 0.1$). Although its fractional contribution was low (25.0 %) compared to Q_{sn} and Q_{rn}, our simulation yielded the largest significant increasing trend value for Q_{sw} ($+12.39$ km^3 yr^{-2}, $p < 0.01$). Among all source waters, Q_{ic} recorded the lowest

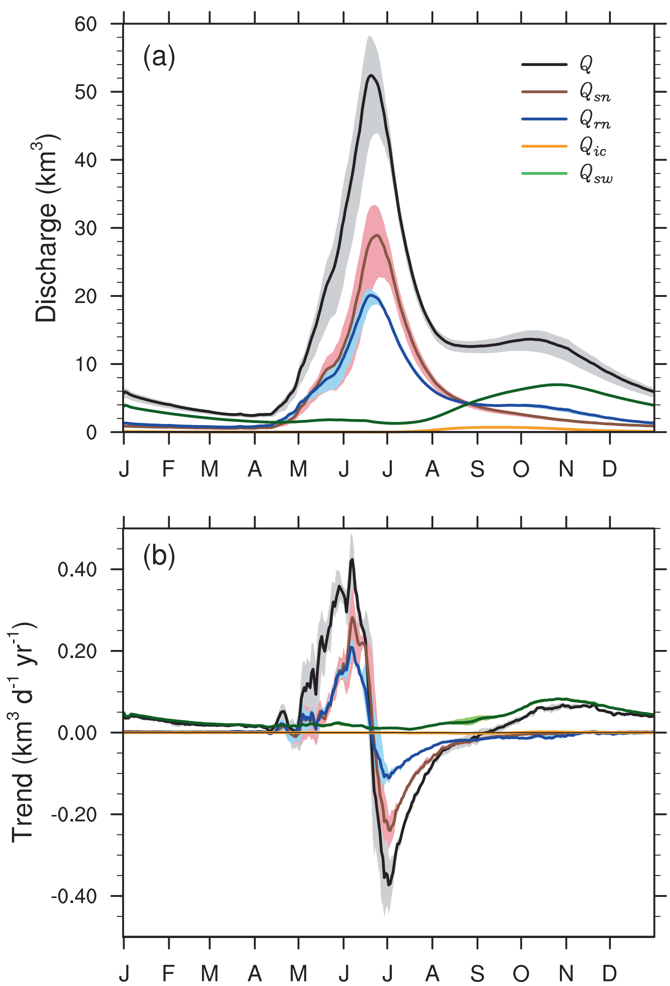

Fig. 10. Seasonal variations in (a) daily discharge and simulated source water distributions for the Arctic circumpolar basin, and (b) corresponding trends over the study period. Shading denotes the range of maximum and minimum values produced by the three meteorological datasets.

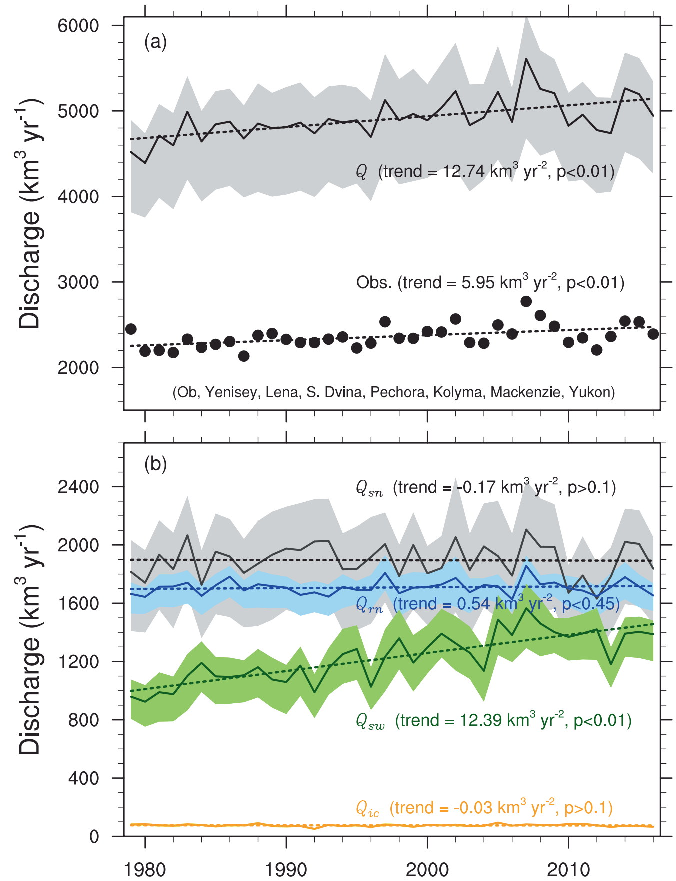

Fig. 11. Interannual variability of (a) discharge from the Arctic circumpolar basin and (b) simulated source water components. Annual total discharge observed for the major eight rivers (Pechora, Severnaya Dvina, Ob, Yenisey, Lena, Kolyma, Yukon, and Mackenzie) is shown in (a) by red dots. Shading denotes the range of maximum and minimum values produced by the three meteorological datasets.

annual volume (75.3 km^3), with a slightly negative (−0.03 km^3 yr^{-1}) but statistically insignificant trend over the study period ($p > 0.1$). The increase of Q_{sw}, particularly over the cold season (Fig. 10b) suggests wetting of the subsurface soil system, likely due to increased precipitation-forced water infiltration from surface layers, enhanced by increased connectivity resulting from permafrost degradation.

3.2.4. Regional difference in river discharge

Annual mean Q from the circumpolar Arctic river basin was simulated to be 4906 km^3 during the study period, and although this is lower than 5169 km^3 calculated by Feng et al. (2021), the simulated results appear to realistically capture regional differences in Q, and importantly, provide new insights into changes in underlying source-water timing and distribution. Overall, we find that the Eurasian River basins produced larger Q than for North America, the difference in volume being 1277.4 km^3, corresponding to 26 % of total Q (Fig. 12), whereas the difference (1402.6 km^3) in observed discharge between the two continents amounted to 58 % of total Q (2396.2 km^3). Underlying source water volumes were also generally larger for the Eurasian River basins, in the range of 5 % to 34 % more than for North America. Enhanced positive trends in simulated Q were found for Eurasia (+8.41 km^3 yr^{-2}) compared to North America (+4.34 km^3 yr^{-2}). However, the trends of Q_{sn} and Q_{rn} (i.e., proportions of source waters) showed different trend directions for the two continents, which is likely inherited from trend differences in parent snowfall and rainfall drivers for each continent. Trend values of Q_{ic} were low for both continents, and although statistically insignificant, appear to reveal some propensity for slightly more positive trends in Eurasia. Overall, Q_{sw} showed the largest and most significant increasing trends for both continents, as captured by the interannual variability (Fig. 11b).

3.2.5. Uncertainty in discharge variables related to forcing datasets

The simulated Q and source waters for the circumpolar Arctic river basin indicated large differences between the three datasets (Supplementary Table 2). The simulations based on CRUNCEP resulted in the lowest Q among the three datasets, including the source waters, which was largely the impact of lower precipitation. For example, Q of CRUNCEP was small 747.2 km^3 yr^{-1}, accounting for − 15 %, compared to the mean value of the three datasets. Meanwhile, WATCH and GSWP were more comparable but above average for Q. Highest values of Q and source water volumes were generated by WATCH, with the exception of Q_{sn} for GSWP, which was 8 % higher (377.4 km^3 yr^{-1}), and Q of WATCH, which was 7 % higher (369.8 km^3 yr^{-1}) than the mean value. Source waters also showed similar patterns as demonstrated by Q. CRUNCEP produced the lowest values for all source waters among the datasets (e.g., –22 % versus mean in Q_{sn}). The reverse case of the highest percentage was + 14 % in Q_{sn} of GSWP. These comparisons represent the highest sensitivity of Q to choice of dataset, and consequently the largest uncertainty in the simulations.

4. Discussion

4.1. Impact of rainwater on ET variability

This study quantitatively assessed the contribution rates of source waters to circumpolar Arctic ET and Q, based on the tracer-aided model simulations using three meteorological forcing datasets. The assessments provided quantitative distribution of source waters for ET and the subcomponents, including their seasonal, interannual, and regional variability that has not obtained from previous studies. Overall, ET was found to be largely accounted for by two source waters, rain (67 %) and snowmelt water (32 %) (Supplementary Table 1), where rain dominated in subarctic boreal forest regions and snow tended to be more prevalent in northern tundra regions (Fig. 5). The latitudinal gradient identified within the spatial distribution of contribution rates was also consistently represented in the ET subcomponents, with the exception of snow sublimation (Supplementary Fig. 2). ET is most active during the warming season. In subarctic regions, warmer climates drive increased ET, with higher rainfall (Fig. 3) further contributing to the greater ET levels. Meanwhile, relatively cold temperatures in northern regions led to increase in the fraction of snowfall in precipitation (Park et al., 2015), which resulted in larger contributions of snowmelt to ET. The model

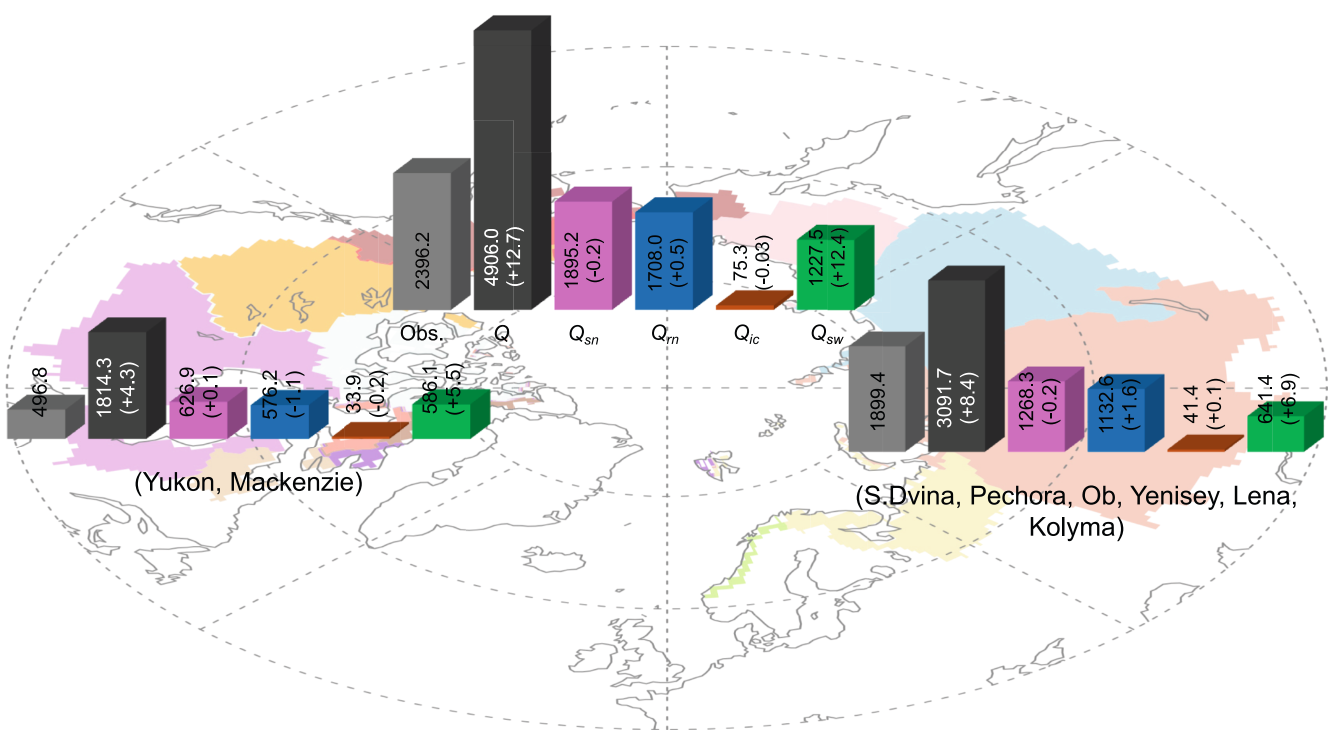

Fig. 12. (Center bar set) Annual discharge and source water partitioning (km^3) to the Arctic Ocean over the study period. Partitioning by geographic origin is also depicted, for North American and Eurasian Rivers (Left and right bar sets, respectively). Trend values (km^3 yr^{-2}) are shown in parentheses.

simulations suggest that the climatic conditions, particularly air temperature, are the primary factor deriving regional differences in the contribution of source waters to *ET*.

The model assessment illustrates that rainwater is a dominant contributor to *ET* and its subcomponents (apart from snow sublimation) (Supplementary Table 1). In the Arctic regions, *ET* is mainly limited by energy except under drought stress (Budyko, 1974), although this is mitigated by rainwater, which serves to reduce water stress controlling stomatal conductance and E^t. The model simulated higher E^t in summer appears to result from higher rainfall (Fig. 3d, see also Supplementary Fig. 3a), with declining latitudinal gradients from the southern boreal forest towards northern tundra regions (Supplementary Fig. 2). Within boreal forest, summer *ET* is found to exceed the rainfall amount (Park et al., 2009), and is therefore unable to meet *ET* water demand. During rainfall events, boreal vegetation is expected to preferentially utilize fresh water from the upper soil layers at rooting depth and may have limited access to groundwater in deeper soil layers (Park et al., 2021a). This may account for the low contribution of soil and permafrost-origin waters to E^t (Supplementary Table 1). In this study, rainwater accounted for 75 % of E^t (Supplementary Table 1). In a comparable study, Miguez-Macho and Fan (2021) assessed plant use for four water source types in model simulations and found that globally and annually, 70 % of plant E^t relied on precipitation. CHANGE also simulated a higher contribution of rainwater to E^s (Supplementary Table 1). In addition, rainfall serves to saturate the soil surface layer during an event, which leads to increase in humidity of the surface layer and reduces vapor pressure deficit, consequently increasing evaporation from the soil surface. The highest contributions of rainwater to E^s were found for the subarctic regions (Supplementary Fig. 2) where snowmelt water contributed approximately 25 % to E^s and E^t (Supplementary Table 1). Contributions of snowmelt water tended to be significant in spring and early summer (Fig. 6a) at times when the water was predominantly being added to the soil surface layers (Park et al., 2021a). Young-Robertson et al. (2016) concluded that deciduous trees transpired 2–30 % of snowmelt water during the growing season, as estimated from volumetric water content in trees measured in a watershed in interior Alaska. These results suggest that the *ET* processes predominantly use water supplied by either rainfall or snowmelt to the surface soil layers during the growing season.

Overall, our simulations revealed an increasing trend for *ET* during the study period (0.38 mm yr^{-2}, $p < 0.01$; Fig. 7a), as a result of the combined impact of warming air temperatures and increased rainfall (0.72 mm yr^{-2}, $p < 0.01$, Fig. 3c), which served to increase available energy and reduce soil water stress, respectively. Warmer air temperature also produced earlier snowmelt and soil thawing in spring (Kim et al., 2012, 2017; Park et al., 2015), which advanced the seasonal timing of vegetation development (Ren et al., 2024) and led to earlier activity of E^s and E^t. Earlier thawing in spring at times when the ground remained frozen promoted runoff but also appeared to remain an important source of E^s and E^t in spring and early summer (Park et al., 2021a), as suggested by increasing trends of ET_{sn} and ET_{rn} and overall *ET* (Fig. 6). Snowmelt during summer mainly occurred at northernmost and high altitudinal mountainous regions. At the scale of the Arctic basin, input of snowmelt water to the soil layers during summer became reduced, while rainfall increased (Fig. 3d). These adjustments resulted in decreasing trends for ET_{sn} and increasing trends for ET_{rn} in summer during the study period (Fig. 6b). We foresee that changes in the seasonal source distributions for *ET* will strengthen under continued warming, with rainwater contributions forming a large proportion of *ET* source water in future.

4.2. Seasonal differences in source water contributions to discharge

Our simulation revealed Q_{sn} to be the dominant source of *Q* overall (39 %; Supplementary Table 2). The contribution of Q_{sn} was most important for the northern cold regions, while Q_{rn} was predominant for subarctic regions, although higher generation rates of Q_{sw} were noted for some areas at the southern boundary of the Arctic basin (Fig. 9). Earlier spring snowmelt when the ground remains frozen is expected to produce higher surface runoff and reduced infiltration to deeper soils, but may increase water storage in shallow layers and promote saturation (Ala-aho et al., 2018). Nevertheless, snowmelt event runoff may also incorporate a high proportion of pre-event water derived from rainwater stored within soil surface layers or depressions. Despite insignificant changes in the annual snowfall totals during the study period (Fig. 3c), Q_{sn} was found to be increasing for spring (Fig. 10b), which is attributed to earlier snowmelt induced by warming air temperatures (Shiklomanov et al., 2007; Tananaev et al., 2016; Suzuki et al., 2020; Hiyama et al., 2023; Park et al., 2024). The accompanying increase in Q_{rn} in spring is partly due to earlier spring rainfall but more significantly reflects higher event-related contributions of autumnal rainfall stored in soil over winter (Park et al., 2024). In summer, both Q_{sn} and Q_{rn} showed significant decreasing trends (Fig. 10b), which is in opposition to trends in overall rainfall, and can be largely attributed to increased *ET* (Fig. 6b), as well as to soil drying in late summer. Drier soils in turn provide more capacity for soil storage of rainfall in late summer and autumn. The result is an effective decrease in connectivity of the surface soil water to runoff in summer. Negative trends observed for Q_{sn} and Q_{rn} persist until autumn, with somewhat greater rates of reduction found for Q_{sn} than for Q_{rn} (Fig. 10b). Negative trends in summer were found to have an impact (although statistically insignificant) on trends of annual Q_{sn} and Q_{rn} during the study period (Fig. 11b). The decreasing trend of Q_{sn} has been observed previously for different regions (Berghuijs et al., 2014; Gordon et al., 2022). Despite insignificant changes in Q_{sn} and Q_{rn}, *Q* showed a significant increasing trend during the study period (12.74 km^3 yr^{-2}, $p < 0.01$, Fig. 11a), which was attributed to the influence of largely increased Q_{sw} (12.39 km^3 yr^{-2}, $p < 0.01$, Fig. 11b). Q_{sw}, manifesting mainly as subsurface runoff, showed positive trends in all seasons, and the increase was significant in autumn and early winter (Fig. 10b). In autumn, the increased net precipitation, caused by the increased precipitation (Fig. 3d) and lower *ET* (Fig. 6a), resulted in larger soil storage, which forced soil water flows downward (Hiyama et al., 2023), resulting in increased subsurface runoff (Evans et al., 2020; Hiyama et al., 2023; Park et al., 2024; Wang et al., 2024). Warming climate also contributed to delay in timing of soil freezing (Kim et al., 2017), which likely was also a factor contributing to higher subsurface runoff production. In autumn, when Q_{sw} was at a maximum, the northern tundra regions had already frozen. Q_{sw} generation mostly occurred within the southern regions with higher rainfall, which contributed in turn to increases in *Q* during the cold season. The increase of Q_{sw} was essentially enhanced by the increased rainfall in autumn (Hiyama et al., 2023). In effect, climate change appears to be increasing the quantity of Arctic river discharge while strengthening contributions of seasonally and regionally different water sources that support *Q*. Climate models have equally projected the increase of rainfall throughout the entire Arctic in the future, particularly in the snow-dominated northern regions and in the autumn period (Bintanja and Andry, 2017). This change likely serves to enhance the connectivity between rainwater and *Q* as well as *ET* (Vihma et al., 2016; Bring et al., 2017; Rawlins and Karmalkar, 2024). The coupling of the net precipitation in autumn to the anomalous runoff in the cold season and spring of the following year is also expected to be amplified in future, most significantly within the cold northern regions.

4.3. Uncertainty and future work

The model-separated source waters in *Q* were compared with the contributions separated by EMMA based on the observations of the Mackenzie River basin (Fig. 8). This comparison points out deficiencies both in representation of sub-permafrost groundwater by CHANGE and uncertainties that persist in defining end members for groundwater used for EMMA. The latter was also verified through sensitivity analyses that tested the effect of altering end member values for groundwater $\delta^{18}O$ (Fig. 8). Despite these limitations and assumptions, EMMA has been shown to be a reasonable approach to partition time-varying contributions from unknown end-member sources. Welp et al. (2005) reported separation results that showed contributions of Q_{sn} and Q_{rn} of 60 % and 40 %, respectively, to annual Q in the Kolyma River basin, using the observed $\delta^{18}O$ and $\delta^{2}H$. The EMMA method has also been applied to river basins of various sizes which provided realistic contribution rates of snowmelt water to Q of 21–44 % for rivers in the Yukon Territory, Canada (Carey and Quinton, 2004; Boucher and Carey, 2010; Carey et al., 2013) and 25–50 % in Northwest Territories and Nunavut, Canada (Gibson et al., 1993; Hayashi et al., 2004; St. Amour et al., 2005). These contribution rates are comparable to our results, which suggest a 39 % contribution rate of Q_{sn} to the circumpolar Arctic basin Q (Supplementary Table 2). In addition, our model results suggested considerable contributions from Q_{sw}, which accounted for 25 % of the Arctic basin Q (Supplementary Table 2). Combining baseflow separation and baseflow index, Wang et al. (2024) separated the contributions of supra-permafrost groundwater to Siberian rivers Q (e.g., Ob, Yenisey, and Lena), which were determined to range from 28.1 % to 39.1 %. Gibson et al. (2016) reported hydrograph separation results based on isotopic data that suggested groundwater accounts for 39 to 50 % of annual Q for three tributaries to the Athabasca River, Canada. While comparisons between our model and field-based assessments is ongoing, results to date suggest that the model serves as a reasonable approximation of hydrologic partitioning within the Arctic basin. Ongoing testing will continue to explore effects associated with differences in climate, landscape, soil, and topography. However, the tracer scheme of CHANGE has certain computational advantages over field-based assessments for practical use in evaluating source water contributions to Q and ET at the scale of the Arctic basin.

The CHANGE model adopts an ice impedance parameter that serves to quantify the tortuosity of the water flow in permafrost as a function of ice content. This parameterization is influential in determining generation of subsurface runoff within the active layer, and serves to limit generation of the groundwater runoff from sub-permafrost zones. Wang et al. (2024) showed sub-permafrost groundwater to account for between 9 and 37 % of Q in the Ob, Yenisey and Lena Rivers. While enhanced permafrost degradation due to climate change (Liljedahl et al., 2016; Ulrich et al., 2017) is expected to increase contributions of the melting ground ice to Q (Park et al., 2021b), our model simulation did not attempt to account for both the impact of excess ice on Q and the sub-permafrost groundwater flows, although this feature is likely a priority of future model improvements, as verified by Fig. 8(c).

Owing to lack of observational results on source waters comprising ET, the simulated ET was compared with global datasets covering the circumpolar Arctic region. The comparison indicated that the CHANGE simulated ET was lower than the value of other global datasets (Fig. 4). This disagreement may be attributed in part to uncertainty of meteorological variables, different model structures and parameterizations, and lack of spatial heterogeneity within the model footprint (Chi et al., 2017; He et al., 2019). The CHANGE-simulated ET revealed smaller differences between the three meteorological forcing datasets (Supplementary Table 1), suggesting that the differences in ET between models were probably associated with the underlying model structures and parameters rather than the meteorological data. In particular, root phenology (i.e., distribution, vertical profile, maximum depth, and seasonal variation), leaf area index dynamics, static vegetation distribution, soil moisture control to E^t, and soil resistance to E^s likely produce large uncertainties in ET (Pan et al., 2020).

The two main limitations of our current assessment should be specifically noted. Firstly, ET simulated by the CHANGE model did not differentiate open water evaporation or the effect of isotopic fractionation by open water evaporation, which is known to influence both isotopic composition and quantity of river discharge in lake and wetland-rich regions (Gibson et al., 2020, 2021a). Secondly, the CHANGE model did not account for modification of water storage and open water evaporation losses associated with thermokarst lake and wetland development, which are known to be changing dynamically across significant areas of Siberia and North America (Liljedahl et al., 2016; Ulrich et al., 2017). Overall, we conclude that these model limitations have led to underestimation of ET in our current assessment, but are identified as important development targets for future model improvement.

5. Conclusions

The tracer-aided model allowed for simulation of the redistribution of source water components under increasing ET and Q trends over the last four decades under changing climate conditions in the Arctic basin. From these simulations we were able to identify spatiotemporal changes in rainwater and groundwater contributions to streamflow, as well as subtle temporal declines in snowmelt water contributions over time. Importantly, the assessments establish that rain plays a key role in driving interannual, seasonal, and regional variability of ET and Q, which appear to be strengthening under changing climate, a pattern of response likely to continue into the future. The influence of changes both due adjustments in seasonality of hydrological processes and the contribution of source waters appears to be amplified by atmospheric feedback, which we postulate may also impact the non-terrestrial environment of the Arctic Ocean including sea ice regimes (see Park et al., 2020). Increased ET appears to be influential in wetting the atmosphere, and also provides positive feedback to precipitation on the terrestrial environment through the regional water recycling. Earlier occurrences of high Q in spring, including the increased cold season Q enhanced by groundwater flow, is also likely to have a direct influence on the overall freshwater budget of the Arctic Ocean. Climate change-induced permafrost degradation and deepening active layer were not found to be significantly linked to the changes in water sources of ET and Q up to the present. However, we point out that the CHANGE model remains limited in its current state by a simple depiction of permafrost dynamics, especially excess ice and sub-permafrost groundwater. Future warming is expected to enhance the melting of ground ice in permafrost, thereby increasing connectivity and dynamics of the hydrological system. Ongoing improvements to model representation for permafrost and ground ice is a priority of future work. Further assessment to test the reality of our intensified water cycle depictions within the Arctic system, including regional variability, is warranted as tracer data availability improves.

CRediT authorship contribution statement

Hotaek Park: Conceptualization, Funding acquisition, Methodology, Formal analysis, Software, Validation, Visualization, Writing – original draft, Writing – review & editing. **Youngwook Kim:** Funding acquisition, Methodology, Formal analysis, Validation, Writing – review & editing. **John Gibson:** Funding acquisition, Data curation, Investigation, Writing – review & editing. **Tetsuya Hiyama:** Funding acquisition, Methodology, Writing – review & editing.

Declaration of competing interest

The authors declare that they have no known competing financial interests or personal relationships that could have appeared to influence the work reported in this paper.

Acknowledgments

This work was conducted as part of the HYPE-ERAS project that is funded by FORMAS (project DNR: 2019-02332), RFBR (project No. 20-55-71005), and JST (Grant No. JPMJBF2003) through the Belmont Forum Collaborative Research Action: Resilience in the Rapidly Changing Arctic. It was also supported by the Japan Society for the Promotion of Science KAKENHI (Grant Numbers 19H05668, 21H04934, 23K25012, and 25H00507), ArCS II (JPMXD1420318865) and ArCS-3 (JPMXD1720251001), InnoTech Alberta Strategic Investment Grant (43110245). We thank A. Shiklomanov for providing observed river discharge data for the comparison of model simulations and two anonymous reviewers for their critical comments and suggestions.

Appendix A. Supplementary data

Supplementary data to this article can be found online at https://doi.org/10.1016/j.jhydrol.2025.134379.

Data availability

Data will be made available on request.

References

Ala-aho, P., Tetzlaff, D., McNamara, J.P., Laudon, H., Kormos, P., Soulsby, C., 2017. Modeling the isotopic evolution of snowpack and snowmelt: testing a spatially distributed parsimonious approach. Water Resour. Res. 53, 5813–5830. https://doi.org/10.1002/2017WR020650.

Ala-aho, P., Soulsby, C., Pokrovsky, O.S., Kirpotin, S.N., Karlsson, J., Serikova, S., et al., 2018. Using stable isotopes to assess surface water source dynamics and hydrological connectivity in a high-latitude wetland and permafrost influenced landscape. J. Hydrol. 556, 279–293. https://doi.org/10.1016/j.jhydrol.2017.11.024.

Allen, R.G., Tasumi, M., Trezza, R., 2007. Satellite-based energy balance for mapping evapotranspiration with internalized calibration (METRIC) - model. J. Irrig. Drain. Eng. 133, 380–394.

Allen, S.T., von Freyberg, J., Weiler, M., Goldsmith, G.R., Kirchner, J.W., 2019. The seasonal origins of streamwater in Switzerland. Geophys. Res. Lett. 46, 10425–10434. https://doi.org/10.1029/2019GL084552.

Aleinov, I., Schmidt, G.A., 2006. Water isotopes in the GISS ModelE land surface scheme. Global Planet. Change 51, 108–120.

AMAP, 2025. Arctic Climate Change Update 2024: Key Trends and Impacts. Summary for Policy-makers. Arctic Monitoring and Assessment Programme (AMAP), Tromsø, Norway. 16 pp.

Amour, N.A., Gibson, J.J., Edwards, T.W.D., Prowse, T.D., Pietroniro, A., 2005. Isotopic time-series partitioning of streamflow components in wetland-dominated catchments, lower Liard River basin, Northwest Territories Canada. Hydrol. Proc. 19, 3357–3381. https://doi.org/10.1002/hyp.5975.

Aron, P.G., Poulsen, C.J., Fiorella, R.P., Matheny, A.M., Veverica, T.J., 2020. An isotopic approach to partition evapotranspiration in a mixed deciduous forest. Ecohydrol 13, e2229.

Arora, V.K., Boer, G.J., 2003. A representation of variable root distribution in dynamic vegetation models. Earth Int. 7, 1–19. https://doi.org/10.1175/1087-3562(2003)007<0001:AROVRD>2.0.CO;2.

Bastiaanssen, W.G.M., Menenti, M., Feddes, R.A., Holtslag, A.A.M., 1998. The surface energy balance algorithm for land (SEBAL): part 1 formulation. J. Hydrol. 212–213, 198–212. https://doi.org/10.1016/S0022-1694(98)00253-4.

Beaudoing, H., Rodell, M., 2016. NASA/GSFC/HSL. GLDAS Noah Land Surface Model L4 monthly 0.25 x 0.25 degree V2.1. Earth Sciences Data and Information Services Center (GES DISC), Greenbelt, Maryland, USA, Goddard. https://doi.org/10.5067/SXAVCZFAQLNO.

Berghuijs, W.R., Woods, R.A., Hrachowitz, M., 2014. A precipitation shift from snow towards rain leads to a decrease in streamflow. Nat. Clim. Chang. 4, 583–586. https://doi.org/10.1038/nclimate2246.

Beria, H., Larsen, J.R., Michelon, A., Ceperley, N.C., Schaefli, B., 2020. HydroMix v1.0: a new Bayesian mixing framework for attributing uncertain hydrological sources. Geosci. Model Dev. 13, 2433–2450. https://doi.org/10.5194/gmd-13-2433-2020.

Bintanja, R., Andry, O., 2017. Towards a rain-dominated Arctic. Nat. Clim. Chang. 7, 263–267. https://doi.org/10.1038/nclimate3240.

Birkel, C., Soulsby, C., 2015. Advancing tracer-aided rainfall–runoff modelling: a review of progress, problems and unrealised potential. Hydrol. Proc. 29, 5227–5240. https://doi.org/10.1002/hyp.10594.

Blaen, P.J., Milner, A.M., Hannah, D.M., Brittain, J.E., Brown, L.E., 2013. Impact of changing hydrology on nutrient uptake in high Arctic rivers. River Res. Appl. 30, 1073–1083. https://doi.org/10.1002/rra.2706.

Boucher, J.L., Carey, S.K., 2010. Exploring runoff processes using chemical, isotopic and hydrometric data in a discontinuous permafrost catchment. Hydrol. Proc. 41, 508–519. https://doi.org/10.2166/nh.2010.146.

Bring, A., Shiklomanov, A., Lammers, R.B., 2017. Pan-Arctic river discharge: prioritizing monitoring of future climate change hot spots. Earth Future 5, 72–92. https://doi.org/10.1002/2016EF000434.

Budyko, M.I., 1974. Climate and life. Academic Press, New York.

Carey, S., Quinton, W., 2004. Evaluating snowmelt runoff generation in a discontinuous permafrost catchment using stable isotope, hydrochemical and hydrometric data. Nord. Hydrol. 35 (4), 309–324.

Carey, S.K., Boucher, J.L., Duarte, C.M., 2013. Inferring groundwater contributions and pathways to streamflow during snowmelt over multiple years in a discontinuous permafrost subarctic environment (Yukon, Canada). Hydrgeol. J. 21 (1), 67–77.

Carrera, J., Vázquez-Suñé, E., Castillo, O., Sánchez-Vila, X., 2004. A methodology to compute mixing ratios with uncertain end-members. Water Resour. Res. 40, 1–11. https://doi.org/10.1029/2003WR002263.

Chi, J., Maureira, F., Waldo, S., Pressley, S.N., Sťockle, C.O., O'Keeffe, P.T., Pan, W.L., Brooks, E.S., Huggins, D.R., Lamb, B.K., 2017. Carbon and water budgets in multiple wheat-based cropping systems in the Inland Pacific Northwest US: comparison of CropSyst simulations with Eddy covariance measurements. Front. Ecol. Evol. 5, 1–18. https://doi.org/10.3389/fevo.2017.00050.

Christophersen, N., Hooper, R.P., 1992. Multivariate analysis of stream water chemical data: the use of principal components analysis for the end-member mixing problem. Water Resour. Res. 28, 99–107.

Delsman, J.R., Oude Essink, G.H., Beven, K.J., Stuyfzand, P.J., 2013. Uncertainty estimation of end-member mixing using generalized likelihood uncertainty estimation (GLUE), applied in a lowland catchment. Water Resour. Res. 49, 4792–4806. https://doi.org/10.1002/wrcr.20341.

Evans, S.G., Yokeley, B., Stephens, C., Brewer, B., 2020. Potential mechanistic causes of increased baseflow across northern Eurasia catchments underlain by permafrost. Hydrol. Proc. 34, 2676–2690. https://doi.org/10.1002/hyp.13759.

Fedorov, A.N., Gavriliev, P.P., Konstantinov, P.Y., Hiyama, T., Iijima, Y., Iwahana, G., 2014. Estimating the water balance of a thermokarst lake in the middle of the Lena River basin, eastern Siberia. Ecohyd 7, 188–196. https://doi.org/10.1002/eco.1378.

Feng, D., Gleason, C.J., Lin, P., Yang, X., Pan, M., Ishitsuka, Y., 2021. Recent changes to Arctic river discharge. Nat. Comm. 12, 6917. https://doi.org/10.1038/s41467-021-27228-1.

Fischer, M.J., 2006. iCHASM, a flexible land-surface model that incorporates stable water isotopes. Global Plan. Change 51, 121–130. https://doi.org/10.1016/j.gloplacha.2005.12.008.

Gibson, J.J., Edwards, T.W.D., Prowse, T.D., 1993. Runoff generation in a high boreal wetland in Northern Canada. Nord. Hydrol. 24 (2–3), 213–224.

Gibson, J. J., Yi, Y., Birks, S. J., 2019. Isotopic tracing of hydrologic drivers including permafrost thaw status for lakes across northeastern Alberta, Canada: a 16-year, 50-lake perspective. J. Hydrol.: Regional Studies 26, 100643 https://doi.org/10.1016/j.ejrh.2019.100643.

Gibson, J.J., Edwards, T.W.D., 2002. Regional water balance trends and evaporation-transpiration partitioning from a stable isotope survey of lakes in northern Canada. Global Biogeo. Cyc. 16, 1026. https://doi.org/10.1029/2001Gb001839.

Gibson, J.J., Yi, Y., Birks, S.J., 2016. Isotope-based partitioning of streamflow in the oil sands region, northern Alberta: towards a monitoring strategy for assessing flow sources and water quality controls. J. Hydrol. Reg. Stud. 5, 131–148. https://doi.org/10.1016/j.ejrh.2015.12.062.

Gibson, J.J., Holmes, T., Stadnyk, T., Birks, S.J., Eby, P., Pietroniro, A., 2020. ^{18}O and ^{2}H in streamflow across Canada. J. Hydrol. Regional Studies 32, 100754. https://doi.org/10.1016/j.ejrh.2020.100754.

Gibson, J.J., Holmes, T., Stadnyk, T., Pietroniro, A., 2021a. Isotopic constraints on water balance and evapotranspiration partitioning in gauged watersheds across Canada. J. Hydrol. Regional Studies 37, 100878. https://doi.org/10.1016/j.ejrh.2021.100878.

Gibson, J.J., Eby, P., Stadnyk, T.A., Holmes, T., Birks, S.J., Pietroniro, A., 2021b. Database of ^{18}O and ^{2}H in streamflow across Canada: a national resource for tracing water sources, water balance and predictive modelling. Data Brief. https://doi.org/10.1016/j.dib.2021.106723.

Gibson, J.J., Jaggi, A., Castrillon-Munoz, F.J., 2025. Widespread pH increase and geochemical trends in fifty boreal lakes: evidence, prediction and plausible attribution to climate and permafrost thaw impacts across northeastern Alberta. J. Hydrol. Regional Studies 58, 102253. https://doi.org/10.1016/j.ejrh.2025.102253.

Goldsmith, G.R., Allen, S.T., Braun, S., Siegwolf, R.T.W., Kirchner, J.W., 2022. Climatic influences on summer use of winter precipitation by trees. Geophys. Res. Lett. 49, e2022GL098323. https://doi.org/10.1029/2022GL098323.

Gordon, B.L., Brooks, P.D., Krogh, S.A., Boisrame, G.F.S., Carroll, R.W.H., McNamara, J. P., Harpold, A.A., 2022. Why does snowmelt-driven streamflow response to warming vary? A data-driven review and predictive framework. Environ. Res. Lett. 17, 053004. https://doi.org/10.1088/1748-9326/ac64b4.

Han, L., Menzel, L., 2022. Hydrological variability in southern Siberia and the role of permafrost degradation. J. Hydrol. 604, 127203. https://doi.org/10.1016/j.jhydrol.2021.127203.

Hathaway, J.M., Westbrook, C.J., Rooney, R.C., Petrone, R.M., Langs, L.E., 2022. Quantifying relative contributions of source waters from a subalpine wetland to downstream water bodies. Hydrol. Proc. 36, e14679. https://doi.org/10.1002/hyp.14679.

Hayashi, M., Quinton, W.L., Pietroniro, A., Gibson, J.J., 2004. Hydrologic functions of wetlands in a discontinuous permafrost basin indicated by isotopic and chemical signatures. J. Hydrol. 296 (1–4), 81–97.

He, M., Kimball, J.S., Yi, Y., Running, S.W., Guan, K., Moreno, A., Wu, X., Maneta, M., 2019. Satellite data-driven modeling of field scale evapotranspiration in croplands using the MOD16 algorithm framework. Remote Sens. Environ. 230, 111201. https://doi.org/10.1016/j.rse.2019.05.020.

Helbig, M., et al., 2020. Increasing contribution of peatlands to boreal evapotranspiration in a warming climate. Nat. Clim. Chang. 10, 555–560. https://doi.org/10.1038/s41558-020-0763-7.

Hessilt, T.D., Rogers, B.M., Scholten, R.C., Potter, S., Janssen, T.A.J., Veraverbeke, S., 2023. Geographically divergent trends in snowmelt timing and fire ignitions across boreal North America. Biogeo 21, 109–129. https://doi.org/10.5194/bg-21-109-2024.

Hiyama, T., Park, H., Kobayashi, K., Lebedeva, L., Gustafsson, D., 2023. Contribution of summer net precipitation to winter river discharge in permafrost zone of the Lena

River basin. J. Hydrol. 616, 128797. https://doi.org/10.1016/j.jhydrol.2022.128797.
Hoeg, S., Uhlenbrook, S., Leibundgut, C., 2000. Hydrograph separation in a mountainous catchment—combining hydrochemical and isotopic tracers. Hydrol. Proc. 14, 1199–1216. https://doi.org/10.1002/(SICI)1099-1085(200005)14:7<1199::AID-HYP35>3.0.CO;2-K.
Hooper, R.P., Christophersen, N., Peters, N.E., 1990. Modelling streamwater chemistry as a mixture of soilwater end-members – an application to the Panola Mountain Catchment, Georgia, U.S.A. J. Hydrol. 116, 321–343.
Hu, H., Dominguez, F., Kumar, P., McDonnell, J., Gochis, D., 2018. A numerical water tracer model for understanding event-scale hydrometeorological phenomena. J. Hydromet. 19, 947–967. https://doi.org/10.1175/JHM-D-17-0202.1.
Jasechko, S., 2019. Global isotope hydrogeology-review. Rev. Geophy. 57, 835–965. https://doi.org/10.1029/2018RG000627.
Jasechko, S., Sharp, Z.D., Gibson, J.J., Birks, S.J., Yi, Y., Fawcett, P.J., 2013. Terrestrial water fluxes dominated by transpiration. Nature 496, 347–350. https://doi.org/10.1038/nature11983.
Jasechko, S., Kirchner, J.W., Welker, J.M., McDonnell, J.J., 2016. Substantial proportion of global streamflow less than three months old. Nat. Geosci. 9, 126–129. https://doi.org/10.1038/ngeo2636.
Jimenez, C., Prigent, C., Mueller, B., Seneviratne, S.I., McCabe, M.F., Wood, E.F., Rossow, W.B., Balsamo, G., Betts, A.K., Dirmeyer, P.A., Fisher, J.B., Jung, M., Kanamitsu, M., Reichle, R.H., Reichstein, M., Rodell, M., Sheffield, J., Tu, K., Wang, K., 2011. Global intercomparison of 12 land surface heat flux estimates. J. Geophy. Res. 116, D02102. https://doi.org/10.1029/2010JD014545.
Kershaw, G.G.L., Wolfe, B.B., English, M.C., 2022. Characterizing seasonal differences in hydrological flow paths and source water contributions to alpine tundra streamflow. Hydrol. Proc. 36, e14775. https://doi.org/10.1002/hyp.14775.
Kim, Y., Kimball, J.S., Zhang, K., McDonald, K.C., 2012. Satellite detection of increasing Northern Hemisphere non-frozen seasons from 1979 to 2008: implications for regional vegetation growth. Remote Sens. Environ. 121, 472–487. https://doi.org/10.1016/j.rse.2012.02.014.
Kim, Y., Kimball, J.S., Glassy, J., Du, J., 2017. An extended global earth system data record on daily landscape freeze-thaw status determined from satellite passive microwave remote sensing. Earth Syst. Sci. Data 9, 133–147. https://doi.org/10.5194/essd-9-133-2017.
Kim, Y., Park, H., Kimball, J.S., Colliander, A., McCabe, M.F., 2023. Global estimates of daily evapotranspiration using SMAP surface and root-zone soil moisture. Remote Sens. Environ. 298, 113803. https://doi.org/10.1016/j.rse.2023.113803.
Kim, Y., Kimball, J.S., Parazoo, N., Xu, X., Colliander, A., Reichle, R., et al., 2024. Diagnosing spring onset across the North American Arctic-boreal region using complementary satellite environmental data records. J. Geophys. Res.: Biogeosci. 129, e2023JG007977. https://doi.org/10.1029/2023JG007977.
Kirchner, J.W., Allen, S.T., 2020. Seasonal partitioning of precipitation between streamflow and evapotranspiration, inferred from end-member splitting analysis. Hydrol. Earth Syst. Sci. 24, 17–39. https://doi.org/10.5194/hess-24-17-2020.
Knighton, J., Souter-Kline, V., Volkmann, T., Troch, P.A., Kim, M., Harman, C.J., et al., 2019. Seasonal and topographic variations in ecohydrological separation within a small, temperate, snow-influenced catchment. Water Resour. Res. 55, 6417–6435. https://doi.org/10.1029/2019WR025174.
Kotani, A., Saito, A., Kononov, A.V., Petrov, R.E., Maximov, T.C., Iijima, Y., Ohta, T., 2019. Impact of unusually wet permafrost soil on understory vegetation and CO2 exchange in a larch forest in eastern Siberia. Agr. For. Meteorol. 265, 295–309. https://doi.org/10.1016/j.agrformet.2018.11.025.
Kuppel, S., Tetzlaff, D., Maneta, M.P., Soulsby, C., 2018. EcH2O-iso 1.0: water isotopes and age tracking in a process-based, distributed ecohydrological model. Geosc. Model Develop. 11, 3045–3069. https://doi.org/10.5194/gmd-11-3045-2018.
Lian, X., Piao, S., Li, L.Z.X., Li, Y., Huntingford, C., Ciais, P., Cescatti, A., Janssens, I.A., Peñuelas, J., Buermann, W., Chen, A., Li, X., Myneni, R.B., Wang, X., Wang, Y., Yang, Y., Zeng, Z., Zhang, Y., McVicar, T.R., 2020. Summer soil drying exacerbated by earlier spring greening of northern vegetation. Sci. Adv. 6, eaax0255.
Liljedahl, A. K., Boike, J., Daanen, R. P., Fedorov, A. N., Frost, G. V., Grosse, G., Hinzman, L. D., Iijma, Y., Jorgenson, J. C., Matveyeva, N., Necsoiu, M., Raynolds, M. K., Romanovsky, V. E., Schulla, J., Tape, K. D., Walker, D. A., Wilson, C. J., Yabuki, H., Zona, D., 2016. Pan-Arctic ice-wedge degradation in warming permafrost and its influence on tundra hydrology. Nat. Geosci. 9, 312–318 https://doi.org/ 10.1038/ngeo2674.
Miguez-Macho, G., Fan, Y., 2021. Spatiotemporal origin of soil water taken up by vegetation. Nature 598, 624–628. https://doi.org/10.1038/s41586-021-03958-6.
Miralles, D.G., Holmes, T.R.H., De Jeu, R.A.M., Gash, J.H., Meesters, A.G.C.A., Dolman, A.J., 2011. Global land-surface evaporation estimated from satellite-based observations. Hydrol. Earth Syst. Sci. 15, 453–469. https://doi.org/10.5194/hess-15-453-2011.
Mudryk, L.R., Kushner, P.J., Derksen, C., Thackeray, C., 2017. Snow cover response to temperature in observational and climate model ensembles. Geophy. Res. Lett. 44, 919–926. https://doi.org/10.1002/2016GL071789.
Nehemy, M.F., Maillet, J., Perron, N., Pappas, C., Sonnentag, O., Baltzer, J.L., et al., 2022. Snowmelt water use at transpiration onset: phenology, isotope tracing, and tree water transit time. Water Resour. Res. 58, e2022WR032344. https://doi.org/10.1029/2022WR032344.
Nelson, J.A., et al., 2024. X-BASE: the first terrestrial carbon and water flux products from an extended data-driven scaling framework. FLUXCOM-x. Biogeos. 21, 5079–5115. https://doi.org/10.5194/bg-21-5079-2024.
Ngo-Duc, T., Oki, T., Kanae, S., 2007. A variable streamflow velocity method for global river routing model: model description and preliminary results. Hydrol. Earth Syst. Sci. Disc. 4, 4389–4414. https://doi.org/10.5194/hessd-4-4389-2007.
Pan, S., Pan, N., Tian, H., Friedlingstein, P., Sitch, S., Shi, H., et al., 2020. Evaluation of global terrestrial evapotranspiration by state-of-the-art approaches in remote sensing, machine learning, and land surface models. Hydrol. Earth Syst. Sci. 24, 1–51. https://doi.org/10.5194/hess-24-1485-2020.
Park, H., Yamazaki, T., Yamamoto, K., Ohta, T., 2008. Tempo-spatial characteristics of energy budget and evapotranspiration in the eastern Siberia. Agri. For. Meteorol. 148, 1990–2005. https://doi.org/10.1016/j.agrformet.2008.06.018.
Park, H., Iijima, Y., Yabuki, H., Ohta, T., Walsh, J., Kodama, Y., Ohata, T., 2011. The application of a coupled hydrological and biogeochemical model (CHANGE) for modeling of energy, water, and CO2 exchanges over a larch forest in eastern Siberia. J. Geophys. Res. 116, D15102. https://doi.org/10.1029/2010JD015386.
Park, H., Walsh, J., Fedorov, A.N., Sherstiukov, A.B., Iijima, Y., Ohata, T., 2013. The influence of climate and hydrological variables on opposite anomaly in active-layer thickness between Eurasian and north American watersheds. Cryosphere 7, 631–645. https://doi.org/10.5194/tc-7-631-2013.
Park, H., Fedorov, A.N., Zheleznyak, M.N., Konstantinov, P.Y., Walsh, J.E., 2015. Effect of snow cover on pan-Arctic permafrost thermal regimes. Clim. Dyn. 44, 2873–2895. https://doi.org/10.1007/s00382-014-2356-5.
Park, H., Kim, Y., Kimball, J.S., 2016a. Widespread permafrost vulnerability and soil active layer increases over the high northern latitudes inferred from satellite remote sensing and process model assessments. Remote Sens. Env. 175, 349–358. https://doi.org/10.1016/j.rse.2015.12.046.
Park, H., Yoshikawa, Y., Oshima, K., Kim, Y., Ngo-Duc, T., Kimball, J.S., Yang, D., 2016b. Quantification of warming climate-induced changes in terrestrial Arctic river ice thickness and phenology. J. Clim. 29, 1733–1754. https://doi.org/10.1175/JCLI-D-15-0569.1.
Park, H., Yoshikawa, Y., Yang, D., Oshima, K., 2017. Warming water in Arctic terrestrial rivers under climate change. J. Hydrom. 18, 1983–1995. https://doi.org/10.1175/JHM-D-16-0260.1.
Park, H., Launiainen, S., Konstantinov, P.Y., Iijima, Y., Fedorov, A.N., 2018. Modeling the effect of moss cover on soil temperature and carbon fluxes at a tundra site in northeastern Siberia. J. Geophys. Res.: Biogeos. 123, 3028–3044. https://doi.org/10.1029/2018JG004491.
Park, H., Watanabe, E., Kim, Y., Polyakov, I., Oshima, K., Zhang, X., Kimball, J.S., Yang, D., 2020. Increasing riverine heat influx triggers Arctic sea ice decline and oceanic and atmospheric warming. Sci. Adv. 6, eabc4699. https://doi.org/10.1126/sciadv.abc4699.
Park, H., Tanoue, M., Sugimoto, A., Ichiyanagi, K., Iwahana, G., Hiyama, T., 2021a. Quantitative separation of precipitation and permafrost waters used for evapotranspiration in a boreal forest: a numerical study using tracer model. J. Geophys. Res.: Biogeos. 126, e2021JG006645. https://doi.org/10.1029/2021JG006645.
Park, H., Fedorov, A.N., Konstantinov, P., Hiyama, T., 2021b. Numerical assessments of excess ice impacts on permafrost and greenhouse gases in a siberian tundra site under a warming climate. Front. Earth Sci. 9, 704447. https://doi.org/10.3389/feart.2021.704447.
Park, H., Hiyama, T., Suzuki, K., 2022. Contribution of water rejuvenation induced by climate warming to evapotranspiration in a Siberian boreal forest. Front. Earth Sci. 10, 1037668. https://doi.org/10.3389/feart.2022.1037668.
Park, H., Kim, Y., Suzuki, K., Hiyama, T., 2024. Influence of snowmelt on increasing Arctic river discharge: numerical evaluation. Prog Earth Planet Sci 11, 13. https://doi.org/10.1186/s40645-024-00617-y.
Popp, A.L., Scheidegger, A., Moeck, C., Brennwald, M.S., Kipfer, R., 2019. Integrating Bayesian groundwater mixing modeling with on-site helium analysis to identify unknown water sources. Water Resour. Res. 55, 10602–10615. https://doi.org/10.1029/2019WR025677.
Pulliainen, J., Luojus, K., Derksen, C., Mudryk, L., Lemmetyinen, J., Salminen, M., Ikonen, J., Takala, M., Cohen, J., Smolander, T., Norberg, J., 2020. Patterns and trends of Northern Hemisphere snow mass from 1980 to 2018. Nature 581, 294–298. https://doi.org/10.1038/s41586-020-2258-0.
Ramankutty, R., Foley, J.A., 1999. Estimating historical changes in global land cover: Croplands from 1700 to 1992. Global Biogeo. Cyc. 13, 997–1027. https://doi.org/10.1029/1999GB900046.
Rawlins, M.A., et al., 2010. Analysis of the arctic system for freshwater cycle intensification: observations and expectations. J. Clim. 23, 5715–5737. https://doi.org/10.1175/2010JCLI3421.1.
Rawlins, M.A., Karmalkar, A.V., 2024. Regime shifts in Arctic terrestrial hydrology manifested from impacts of climate warming. Cryosphere 18, 1033–1052. https://doi.org/10.5194/tc-18-1033-2024.
Ren, Y., Qiu, J., Zeng, Z., Liu, X., Sitch, S., Pilegaard, K., Yang, T., Wang, S., Yuan, W., Jain, A.K., 2024. Earlier spring greening in Northern Hemisphere terrestrial biomes enhanced net ecosystem productivity in summer. Comm. Earth Environ. 5, 122. https://doi.org/10.1038/s43247-024-01270-5.
Risi, C., et al., 2016. The water isotopic version of the land-surface model ORCHIDEE: implementation, evaluation, sensitivity to hydrological parameters. Hydrol. Curr. Res. 7, 258. https://doi.org/10.4172/2157-7587.1000258.
Senay, G.B., Bohms, S., Singh, R., Gowda, P.A., Velpuri, N.M., Alemu, H., Verdin, J.P., 2013. Operational evapotranspiration mapping using remote sensing and weather datasets: a new parameterization for the SSEB approach. J. Amer. Water Resour. Assoc. 49 (3), 577–591.
Shiklomanov, A.I., Lammers, R.B., Rawlins, M.A., Smith, L.C., Pavelsky, T.M., 2007. Temporal and spatial variations in maximum river discharge from a new Russian dataset. J. Geophys. Res. 112, G04S53. https://doi.org/10.1029/2006JG000352.
Smith, L.C., Pavelsky, T.M., MacDonald, G.M., Shiklomanov, A.I., Lammers, R.B., 2007. Rising minimum daily flows in northern Eurasian rivers: a growing influence of

groundwater in the high-latitude hydrologic cycle. J. Geophys. Res. 112 (G4), G04S47. https://doi.org/10.1029/2006JG000327.
Soulsby, C., Birkel, C., Geris, J., Dick, J., Tunaley, C., Tetzlaff, D., 2015. Stream water age distributions controlled by storage dynamics and nonlinear hydrologic connectivity: Modeling with high-resolution isotope data. Water Resour. Res. 51 (9), 7759–7776. https://doi.org/10.1002/2015WR017888.
Sprenger, M., Allen, S.T., 2020. What ecohydrologic separation is and where we can go with it. Water Resour. Res. 56, e2020WR027238. https://doi.org/10.1029/2020WR027238.
Sprenger, M., Carroll, R.W.H., Dennedy-Frank, J., Siirila-Woodburn, E.R., Newcomer, M. E., Brown, W., et al., 2022. Variability of snow and rainfall partitioning into evapotranspiration and summer runoff across nine mountainous catchments. Geophys. Res. Lett. 49, e2022GL099324. https://doi.org/10.1029/2022GL099324.
Stadnyk, T.A., Holmes, T.L., 2023. Large scale hydrologic and tracer aided modelling: a review. J. Hydrol. 618, 129177. https://doi.org/10.1016/j.jhydrol.2023.129177.
St Amour, N.A., Gibson, J.J., Edwards, T.W.D., Prowse, T.D., Pietroniro, A., 2005. Isotopic time-series partitioning of streamflow components in wetlanddominated catchments, lower Liard River basin, Northwest Territories Canada. Hydrol. Process. 19 (17), 3357–3381.
Sturm, C., Zhang, Q., Noone, D., 2010. An introduction to stable water isotopes in climate models: benefits of forward proxy modelling for paleoclimatology. Clim. Past 6, 115–129. https://doi.org/10.5194/cp-6-115-2010.
Suzuki, K., Hiyama, T., Matsuo, K., Ichii, K., Iijima, Y., Yamazaki, D., 2020. Accelerated continental-scale snowmelt and ecohydrological impacts in the four largest Siberian river basins in response to spring warming. Hydrol. Proc. 34, 3867–3881. https://doi.org/10.1002/hyp.13844.
Tananaev, N.I., Makarieva, O.M., Lebedeva, L.S., 2016. Trends in annual and extreme flows in the Lena River basin, Northern Eurasia. Geophys. Res. Lett. 43, 10764–10772. https://doi.org/10.1002/2016GL070796.
Terzer-Wassmuth, S., Araguás-Araguás, L.J., Copia, L., Wassenaar, L.I., 2022. High spatial resolution prediction of tritium (^{3}H) in contemporary global precipitation. Sci. Rep. 12, 10271. https://doi.org/10.1038/s41598-022-14227-5.
Tetzlaff, D., Buttle, J., Carey, S.K., Kohn, M.J., Laudon, H., McNamara, J.P., et al., 2020. Stable isotopes of water reveal differences in plant – soil water relationships across northern environments. Hydrol. Proc. 35, e14023. https://doi.org/10.1002/hyp.14023.
Ulrich, M., Matthes, H., Schirrmeister, L., Schütze, J., Park, H., Iijima, Y., Fedorov, A.N., 2017. Differences in behavior and distribution of permafrost-related lakes in Central Yakutia and their response to climatic drivers. Water Resour. Res. 53, 1167–1188. https://doi.org/10.1002/2016WR019267.
Vihma, T., Screen, J., Tjernström, M., Newton, B., Zhang, X., Popova, V., Deser, C., Holland, M., Prowse, T., 2016. The atmospheric role in the Arctic water cycle: a review on processes, past and future changes, and their impacts. J. Geophys. Res. Biogeo. 121, 586–620. https://doi.org/10.1002/2015JG003132.
Walvoord, M.A., Kurylyk, B.L., 2016. Hydrologic impacts of thawing permafrost–a review. Vad. Zone J. 15, 1–20. https://doi.org/10.2136/vzj2016.01.0010.
Walvoord, M.A., Striegl, R.G., 2007. Increased groundwater to stream discharge from permafrost thawing in the Yukon River basin: potential impacts on lateral export of carbon and nitrogen. Geophys. Res. Lett. 34, L12402. https://doi.org/10.1029/2007GL030216.
Wan, C., Gibson, J.J., Shen, S., Yi, Y., Yi, P., Yu, Z., 2019a. Using stable isotopes paired with tritium analysis to assess thermokarst lake water balances in the Source Area of the Yellow River, northeastern Qinghai-Tibet Plateau China. Sci. Total Environ. 689, 1276–1292. https://doi.org/10.1016/j.scitotenv.2019.06.427.
Wan, C., Li, K., Shen, S., Gibson, J.J., Ji, K., Yi, P., Yu, Z., 2019b. Using tritium and 222Rn to estimate groundwater discharge and thawing permafrost contributing to surface water in permafrost regions on Qinghai - Tibet Plateau. J. Radioanal. Nuc. Chem. 322, 561–578. https://doi.org/10.1007/s10967-019-06720-5.
Wan, C., Gibson, J.J., Peters, D.L., 2020. Isotopic constraints on water balance of tundra lakes and watersheds disturbed by permafrost degradation in the Mackenzie Delta region, Northwest Territories Canada. Sci. Total. Environ. 731, 139176. https://doi.org/10.1016/j.scitotenv.2020.139176.
Wang, L., Wu, B., Elnashar, A., Zeng, H., Zhu, W., Yan, N., 2021a. Synthesizing a regional territorial evapotranspiration dataset for northern China. Remote Sens. 13 (6), 1076. https://doi.org/10.3390/rs13061076.
Wang, P., Huang, Q., Pozdniakov, S.P., Liu, S., Ma, N., Wang, T., et al., 2021b. Potential role of permafrost thaw on increasing Siberian river discharge. Environ. Res. Lett. 16, 034046. https://doi.org/10.1088/1748-9326/abe326.
Wang, R., Li, L., Gentine, P., Zhang, Y., Chen, J., Chen, X., Chen, L., Ning, L., Yuan, L., Lü, G., 2022. Recent increase in the observation-derived land evapotranspiration due to global warming. Environ. Res. Lett. 17, 024020. https://doi.org/10.1088/1748-9326/ac4291.
Wang, Z., Sun, S., Wang, G., Song, C., 2024. Spatial-temporal differentiation of supra- and sub-permafrost groundwater contributions to river runoff in the Eurasian Arctic and Qinghai-Tibet Plateau permafrost regions. Water Resour. Res. 60, e2023WR035913. https://doi.org/10.1029/2023WR035913.
Welp, L., Randerson, J., Finlay, J., Davydov, S., Zimova, G., Davydova, A., et al., 2005. A high-resolution time series of oxygen isotopes from the Kolyma River: implications for the seasonal dynamics of discharge and basin-scale water use. Geophys. Res. Lett. 32, L14401. https://doi.org/10.1029/2005GL022857.
White, D., et al., 2007. The arctic freshwater system: changes and impacts. J. Geophys. Res. 112, G04S54. https://doi.org/10.1029/2006JG000353.
Whitman, T., Lehmann, J., 2015. A dual-isotope approach to allow conclusive partitioning between three sources. Nat. Comm. 6, 8708. https://doi.org/10.1038/ncomms9708.
Wu, Z., Huang, N. E., Long, S. R., Peng, C.-K., 2007. On the trend, detrending, and variability of nonlinear and nonstationary time series. Proc. Nat. Acad. Sci. 104(38), 14889–14894 https://doi.org/ 10.1073/pnas.0701020104.
Yang, Y., Roderick, M.L., Guo, H., Miralles, D.G., Zhang, L., et al., 2023. Evapotranspiration on a greening earth. Nat. Rev. Earth Environ. 4, 626–641. https://doi.org/10.1038/s43017-023-00464-3.
Yi, Y., Gibson, J. J., Cooper, L. W., Hélie J.-F., Birks, S. J., McClelland, J. W., Holmes, R. M., Peterson, B. J., 2012. Isotopic signals (^{18}O, ^{2}H, ^{3}H) of six major rivers draining the pan-Arctic watershed. Global Biogeo. Cyc. 26, GB1027 https://doi.org/10.1029/2011GB004159.
Yoshimura, K., Miyazaki, S., Kanae, S., Oki, T., 2006. Iso-MATSIRO, a land surface model that incorporates stable water isotopes. Global Plan. Change. 51, 90–107. https://doi.org/10.1016/j.gloplacha.2005.12.007.
Young-Robertson, J.M., Bolton, W.R., Bhatt, U.S., Cristobal, J., Thoman, R., 2016. Deciduous trees are a large and overlooked sink for snowmelt water in the boreal forest. Sci. Rep. 6, 29504. https://doi.org/10.1038/srep29504.
Zhang, K., Kimball, J.S., Mu, Q., Jones, L.A., Goetz, S.J., Running, S.W., 2010. Satellite based analysis of northern ET trends and associated changes in the regional water balance from 1983 to 2005. J. Hydrol. 379, 92–110. https://doi.org/10.1016/j.jhydrol.2009.09.047.
Zhang, Q., Knowles, J.F., Barnes, R.T., Cowie, R.M., Rock, N., Williams, M.W., 2018. Surface and subsurface water contributions to streamflow from a mesoscale watershed in complex mountain terrain. Hydrol. Proc. 32, 954–967. https://doi.org/10.1002/hyp.11469.